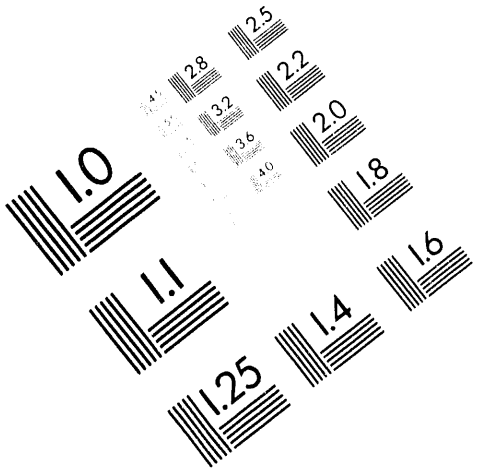

Association for Information and Image Management

1100 Wayne Avenue, Suite 1100
Silver Spring, Maryland 20910

301/587-8202

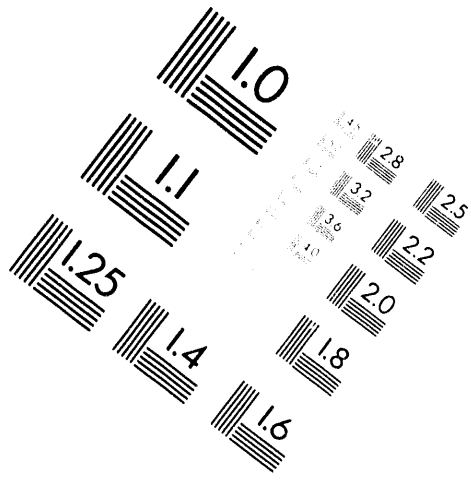

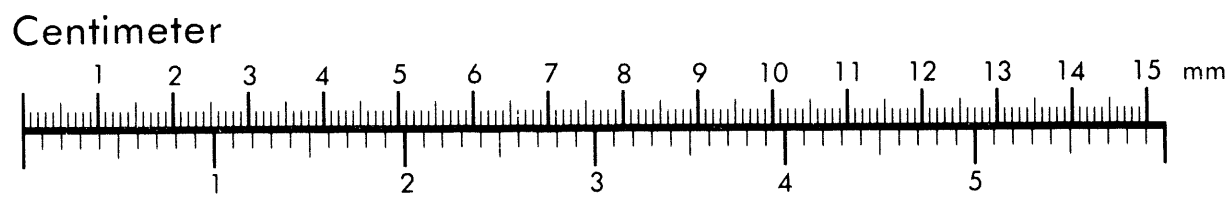

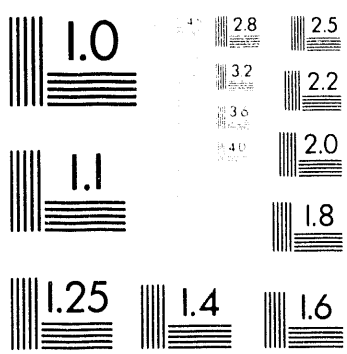

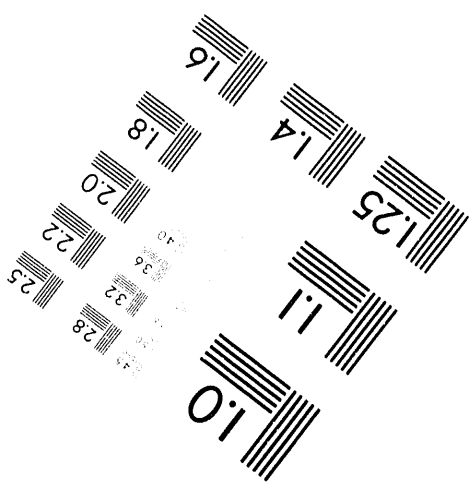

MANUFACTURED TO AIIM STANDARDS
BY APPLIED IMAGE, INC.

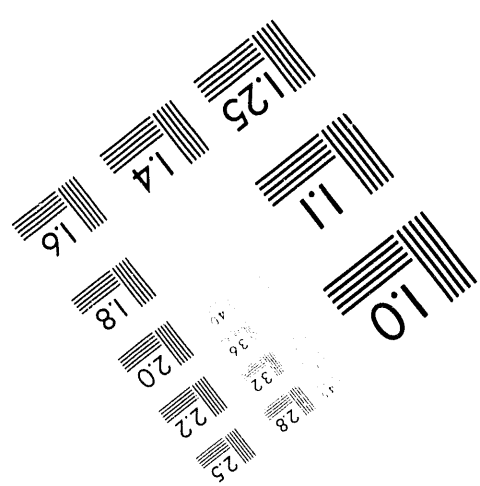

1 of 1

DOE/ER/13749-T2

I. PROGRESS REPORT

Ultrasonic evaluation of porous materials can take advantage of some very specific acoustic phenomena which occur only in fluid-saturated consolidated solids of continuously connected pore structure. Certain material properties of the porous frame such as the degree of consolidation or grain size can be readily evaluated from the velocity or attenuation of the shear and longitudinal waves in the dry skeleton or those of the fast compressional wave in the fluid-saturated material.[1,2] Other parameters such as tortuosity, permeability, porosity, and pore size, shape and surface quality are inherently connected to the porous nature of the material and can be evaluated much better from the propagation properties of the slow compressional wave. Unfortunately, the slow compressional wave is usually very weak due to high attenuation caused by viscous drag between the fluid and the solid frame. In natural rocks, the viscous drag is further increased by the highly irregular pore structure as well as by impurities such as clay particles deposited both within the pore throats and on the surfaces of the rock grains.[3] The excessive attenuation results in the complete disappearance of the slow compressional mode in water-saturated rocks. Because of this, we have to introduce two novel experimental approaches which are more suitable to geophysical applications where the economic benefits of ultrasonic material characterization are enormous.

First, we studied bulk slow wave propagation in air-filled porous materials. Due to the relatively high kinematic viscosity of air, the slow compressional wave is even more attenuated than in water-saturated samples, but it is the only mode which is generated with a significant amplitude, therefore its detection is fairly simple. Second, we also studied the feasibility of using different surface modes to characterize the properties of water-saturated rocks. This technique is based on the indirect observation of the slow compressional wave through its significant effect on the velocity of the surface mode propagating along the free surface of the wet rock. The main results of these two research efforts are discussed separately in the following chapters.

1.1 AIR-SATURATION TECHNIQUE

The most interesting feature of acoustic wave propagation in fluid-saturated porous media is the appearance of a second compressional wave, the so-called slow wave. The existence of a slow compressional wave in an isotropic and macroscopically homogeneous fluid-saturated porous medium was predicted by Biot in 1956.[4,5] The main characteristic of this mode is that its

DISCLAIMER

velocity is always lower than both compressional wave velocities in the fluid and solid frame. Below a critical frequency, which depends on the pore size in the frame and the kinematic viscosity of the fluid, the slow compressional wave is highly dispersive and strongly attenuated over a single wavelength. Above this critical frequency, it becomes a dispersion-free propagating wave with fairly low attenuation that slightly increases with frequency. The slow compressional wave represents a relative motion between the fluid and the solid frame. This motion is very sensitive to the kinematic viscosity of the fluid and the dynamic permeability of the porous formation. Naturally, low-viscosity liquids such as water are the fluids most often used in such experiments. In our current research effort, we have been studying the feasibility of using gaseous fluids such as air to saturate the porous specimens.

1.1.1 INTRODUCTION AND BACKGROUND

Since 1980, when Plona was able to observe slow wave propagation in artificial rocks made of sintered glass beads,[6] the question of why slow waves cannot be detected in real rocks has been one of the major issues in the acoustics of fluid-saturated materials. One of the main reasons is obviously the high degree of geometrical disorder in such materials, which results in rather uneven flow patterns thereby greatly increasing viscous drag. In addition, Klimenatos and McCann showed that the lack of perceivable slow wave propagation is also due to inherent internal impurities, such as submicron clay particles, found in all types of natural rocks.[3] These clay particles, deposited both within the pore throats and on the surfaces of the rock grains, greatly increase viscous drag between the fluid and solid frame, which results in excessive attenuation and usually complete disappearance of the slow wave. One way to reduce the excessive attenuation of slow waves in porous materials is to use special fluids of very low viscosity to saturate the specimen. For instance, superfluid ^{4}He below 1.1K has been shown to work very well in fused glass bead samples,[7] superleak materials consisting of compacted powders,[8-10] and in sandstones,[11] but the technique is obviously very cumbersome.

The question of whether or not excessive attenuation in viscous fluid-saturated natural rocks renders the detection of slow waves impossible arises. Not necessarily! Even a very weak slow wave, attenuated by as much as 50-60 dB, could easily be detected but for the presence of much stronger background "noise" caused by the direct arrivals and scattered components of the fast compressional and/or shear waves. If we could generate the slow wave only and nothing else, it would be much easier to detect in spite of the substantial attenuation. Compared to the solid frame, liquids like water usually have a lower, but still comparable density ρ_f and bulk modulus

B_f. Although their viscosity μ is also relatively high, which makes saturation of the porous sample somewhat troublesome, their kinematic viscosity $\eta = \mu/\rho_f$ is fairly low. On the other hand, gaseous fluids like air have very low density, bulk modulus, and viscosity, while their kinematic viscosity is usually rather high. Therefore, it is very simple to saturate a porous sample by air, but the slow wave is expected to be highly dispersive and strongly attenuated. In spite of these adverse effects, slow waves can be readily observed in air-filled porous samples, including certain natural rocks, by using airborne ultrasonic waves.[12]

In the case of air saturation, because of the tremendous acoustical mismatch between the incident compressional wave and the porous solid, all the incident energy is either reflected or transmitted via the slow wave without generating appreciable fast compressional or shear transmitted waves. In order to demonstrate this crucial effect, Figure 1 shows the slow, fast, and shear wave transmission coefficients through water- and air-saturated glass bead specimens. The physical parameters of the glass bead specimen and details of the calculation are given in Ref. 13. In the case of water saturation, the slow compressional wave is usually 5-10 dB weaker than the fast compressional or shear modes and it is much more attenuated. Also, because of its lower velocity, it arrives later than the other modes and it is often overshadowed by multiple reflections and scattered components of these stronger signals. Maybe the only exception is when the shear velocity is sufficiently high so that we can work above the second critical angle where the slow compressional wave becomes the only propagating mode in the fluid-saturated sample (unfortunately, this does not happen in most natural rocks where the shear velocity is rather low). On the other hand, in the case of air saturation, the slow compressional wave is at least 70 dB stronger than all other modes and, due to the very low sound velocity in air, the shear critical angle drops below 15°, above which only the slow wave is transmitted through the sample. This means that the highly attenuated slow wave will be submerged in electrical noise rather than spurious signals so it can be easily recovered by simple time-averaging.

Our slow wave inspection technique is based on the transmission of airborne ultrasonic waves through air-filled porous plates.[12] Figure 2 shows the block diagram of the experimental system used in this study. Standard ultrasonic NDE equipment was used without any particular effort to obtain high generation or detection sensitivity. The rather poor coupling between the applied contact transducers and air resulted in a rather low, but fairly constant, sensitivity over a wide frequency range of 50-500 kHz. In certain cases, we replaced the ultrasonic transmitter and receiver by a commercial tweeter and electret microphone, respectively, so that measurements could be done between 10 kHz and 50 kHz, too.

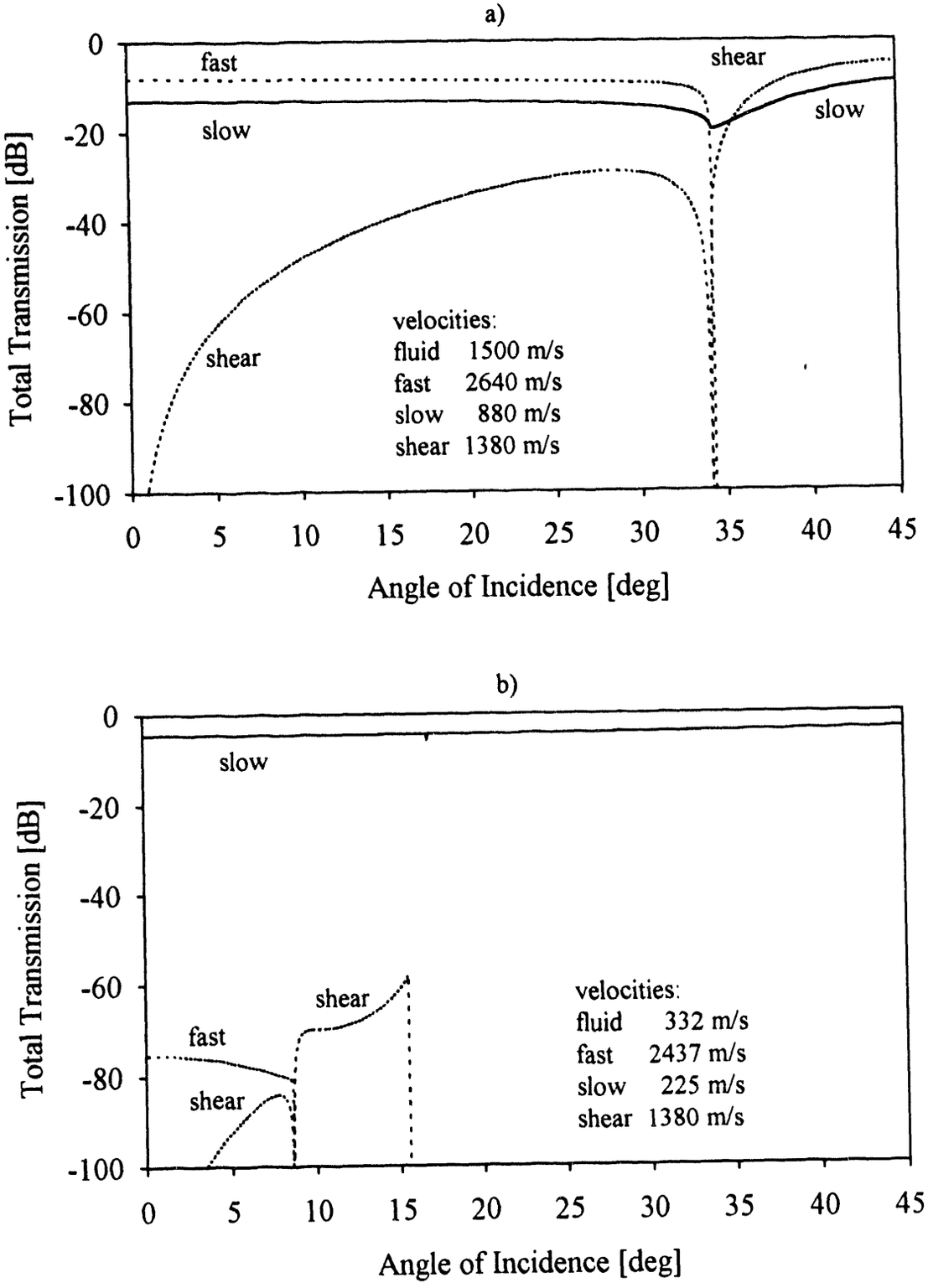

Figure 1 Slow, fast, and shear transmission coefficients through (a) water- and (b) air-saturated porous glass bead plates.

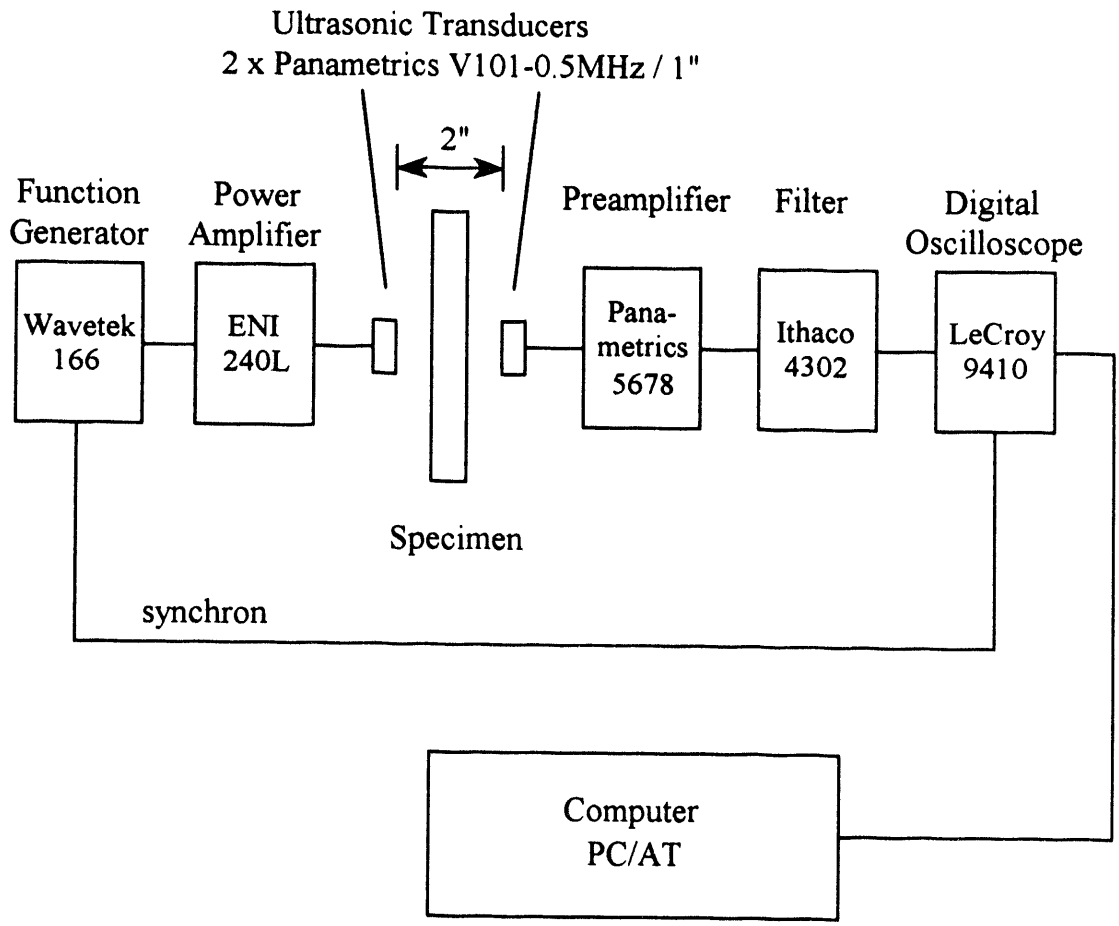

Figure 2 Block diagram of the experimental system.

In order to assure an acceptable signal-to-noise ratio, extensive signal averaging is used, up to 10^5 samples. The transmitter is driven by a tone-burst of five cycles. The received signals with and without the specimen placed between the transducers are digitally stored. Then the computer selects the first five cycles of the signal, from which determines the insertion loss L_i and insertion delay t_i. The insertion loss is calculated from the Fourier components of the gated signals at the carrier frequency. The insertion delay is determined by finding the maximum of the cross-correlation function of the two signals. The thickness of the specimens is usually varied between 1 and 5 mm to accommodate different permeabilities over the widest possible frequency range. Because of the very high attenuation in these samples, resonance peaks in the transmission are generally very weak but sometimes, especially at lower frequencies, faintly visible. The samples are typically 4" in diameter and, especially certain inherently inhomogeneous natural rocks, show

significantly uneven attenuation distribution within this area. The experimental data usually include 50 - 250 measurements taken at randomly chosen positions as the frequency is scanned up and down within the usable range.

This technique can be readily used to study the frequency-dependent velocity and attenuation of the slow compressional wave in different porous materials including natural rocks in both low-frequency (diffuse) and high-frequency (propagating) regimes. Our experimental results on the propagation properties of slow compressional waves in air-filled synthetic and natural rocks were recently published in a detailed paper.[14] Generally, we found good agreement between existing theoretical predictions and the measured velocity and attenuation except for an anomalous excess attenuation at very high frequencies. In the diffuse region, which is usually below 100 kHz, both the velocity and the attenuation coefficient are primarily determined by the static permeability of the material. In the propagating region, the velocity depends on the tortuosity only while the attenuation coefficient exhibits an anomalously high attenuation which depends on the size-distribution and shape of the pores.

As a typical example, Figure 3 shows the normalized slow wave velocity and attenuation coefficient in a 1.5-mm-thick Berea Sandstone specimen of 200 mD static permeability. The experimentally measured velocity agrees quite well with the analytical results while the attenuation exhibits higher-than-predicted attenuation and more or less linear frequency-dependence. In the diffuse regime, i. e., at low frequencies, the velocity and the attenuation coefficient contain the same information on the permeable formation. The attenuation is linearly while the velocity is inversely proportional to the square-root of $\phi s_p^2/\kappa_0$,where ϕ is the porosity, κ_0 is the static permeability and s_p is the pore shape factor ratio introduced by Attenborough.[15,16] Since the static permeability κ_0 and the pore shape factor ratio s_p always occur in the same combination through the normalized pore radius ξ, they cannot be separated by acoustical measurements. Instead, κ_0/s_p^2 was used to define a new material parameter, the so-called acoustic permeability κ_a, which can be determined from the low-frequency propagation parameters of the slow compressional wave

$$\kappa_a = \frac{\kappa_o}{4\gamma s_p^2} . \qquad (1)$$

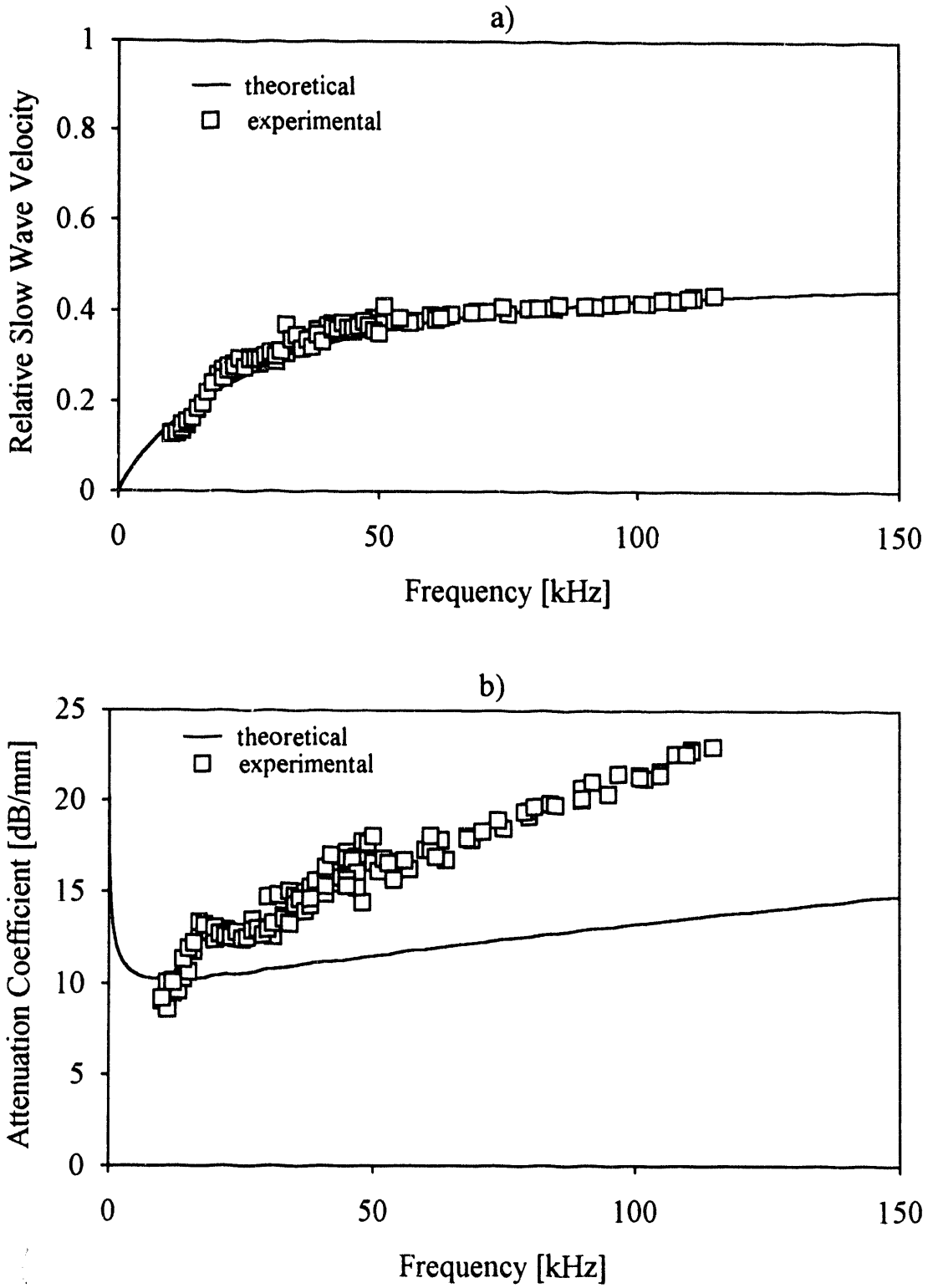

Figure 3 Normalized slow wave velocity (a) and attenuation coefficient (b) in a 1.5-mm-thick Berea Sandstone specimen of 200 mD static permeability.

Comparison of the acoustic permeability κ_a and the static permeability κ_o yields valuable information on the geometry of the pore space. We found that, for cemented glass beads, the pore shape factor ratio is between 0.4 and 0.475, i. e., very close to the theoretically possible highest value of 0.5. In comparison, for different natural rocks studied in this work, the pore shape factor ratio was found to be much lower between 0.2 and 0.3.[14] Although the porosity ϕ is most easily determined by simple weight measurements on the dry and wet sample, it should be mentioned that it can be assessed by purely acoustical means, too. This is possible because both real and imaginary parts of the acoustical impedance are proportional to the square-root of $s_p^2/\kappa_o\phi$, and s_p^2/κ_o can be determined from the velocity or the attenuation coefficient of the slow wave, which are not affected directly by the porosity. In the diffuse regime, the acoustic impedance can be readily determined by reflection measurements.[17,18]

In the propagating regime, i. e., at high frequencies, only the velocity seems to be in good agreement with the theoretical predictions. Anyway, the velocity by itself is sufficient to determine the high-frequency tortuosity τ_∞ of the material while the attenuation coefficient would provide only redundant information on $s_p^2/\kappa_o\phi$ which is better determined from the low-frequency behavior. Still, it is expected that the excess high-frequency attenuation contains valuable additional information on the geometry of the pore space and the surface roughness of the pore channels therefore it is of great importance to understand the underlying physical process which causes the observed loss. Therefore, our main effort in connection with the further development of the air-saturation technique was directed at identifying the attenuation mechanism responsible for the excess loss.

1.1.2 ATTENUATION MECHANISM

Our previous experimental results indicated that the attenuation coefficient of the slow compressional wave in air-filled porous solids always approaches a linear slope at high frequencies. This effect represents a significant excess attenuation above the theoretically predicted viscous loss which is proportional to only the square-root of frequency. According to our measurements, this slope is determined by the shape of the pore channels and the degree of geometrical disorder in the material, but essentially independent of size. In the case of linearly frequency-dependent attenuation coefficient, the actual loss is best measured by the so-called normalized attenuation, α_n, or by its inverse, the quality factor. The normalized attenuation is the total attenuation over one wavelength. In the low-frequency diffuse regime, the normalized

attenuation is constant at $\alpha_n = 2\pi$ Neper $\approx$ 57 dB. At the transition between the diffuse and propagating regimes, the normalized attenuation starts to decrease and approaches a lower asymptotic value at high frequencies. According to our experimental results from glass bead specimens, the high-frequency normalized attenuation is constant at $\alpha_n \approx 8.3$ dB regardless of the diameter of the beads over almost one decade. These samples are cemented from spherical glass beads of different diameters and all have approximately the same porosity, tortuosity and pore geometry, therefore they can be used as an almost ideal self-similar porous solid to study separately shape and size effects. Figure 4 shows the measured attenuation versus frequency curves in five different grades of cemented glass beads (grade designations used to identify EP Brand Porous Structures denote the maximum interstitial pore diameter in microns).

Similar measurements in other materials showed that the normalized attenuation increases for more irregular pore geometries. Figure 5 shows the high-frequency limit of the normalized attenuation in a number of synthetic and natural rock materials. The sintered bronze specimens (B10 and B40 of Ref. 2) had regular spherical shaped beads and roughly 25 % connected porosity ($\alpha_n \approx 9.4$ dB). The sintered steel specimens (S10 and S40 of Ref. 2) contained 31 % porosity but exhibited very strongly distorted grain particles and irregular pore shapes, which explains the increase in normalized attenuation ($\alpha_n \approx 13.3$ dB). The highest loss was observed in natural rocks where the high-frequency normalized attenuation reaches $\alpha_n \approx 19$ - 23 dB, i. e., almost three times higher than in the most regular cemented glass bead specimens. Naturally, these are averaged values for all specimens over their entire cross-sections, and, considering the significant local variations, the actual change can be even larger.

Since, at least in the upper part of the frequency range, the grain size is comparable to the wavelength, the excess attenuation could be caused by elastic scattering. For example, the diameter of the cemented glass beads in grade 175 is $d_g \approx 600$ μm, i. e., $kd_g > 1$ above 60 kHz. Unfortunately, at this point, there seems to be no theoretical prediction available in the literature for the scattering induced attenuation of the slow compressional wave in permeable solids. In a recent paper, Chaban suggested a new inhomogeneous attenuation model for acoustic wave propagation in sediments and rocks, which takes into account the presence of large-scale inhomogeneities by assuming macroscopic diffusion.[19] Rays propagating along different paths arrive at the reception point with different phases. Assuming that the resulting phase distribution is a Lorentzian one (a somewhat artificial restriction), this mechanism yields strong attenuation without velocity dispersion and the attenuation coefficient is linearly proportional to frequency. At first sight, this mechanism is the acoustic equivalent of the hydrodynamic dispersion observed in porous media. On the other hand, Chaban's theory predicts a linearly frequency-dependent

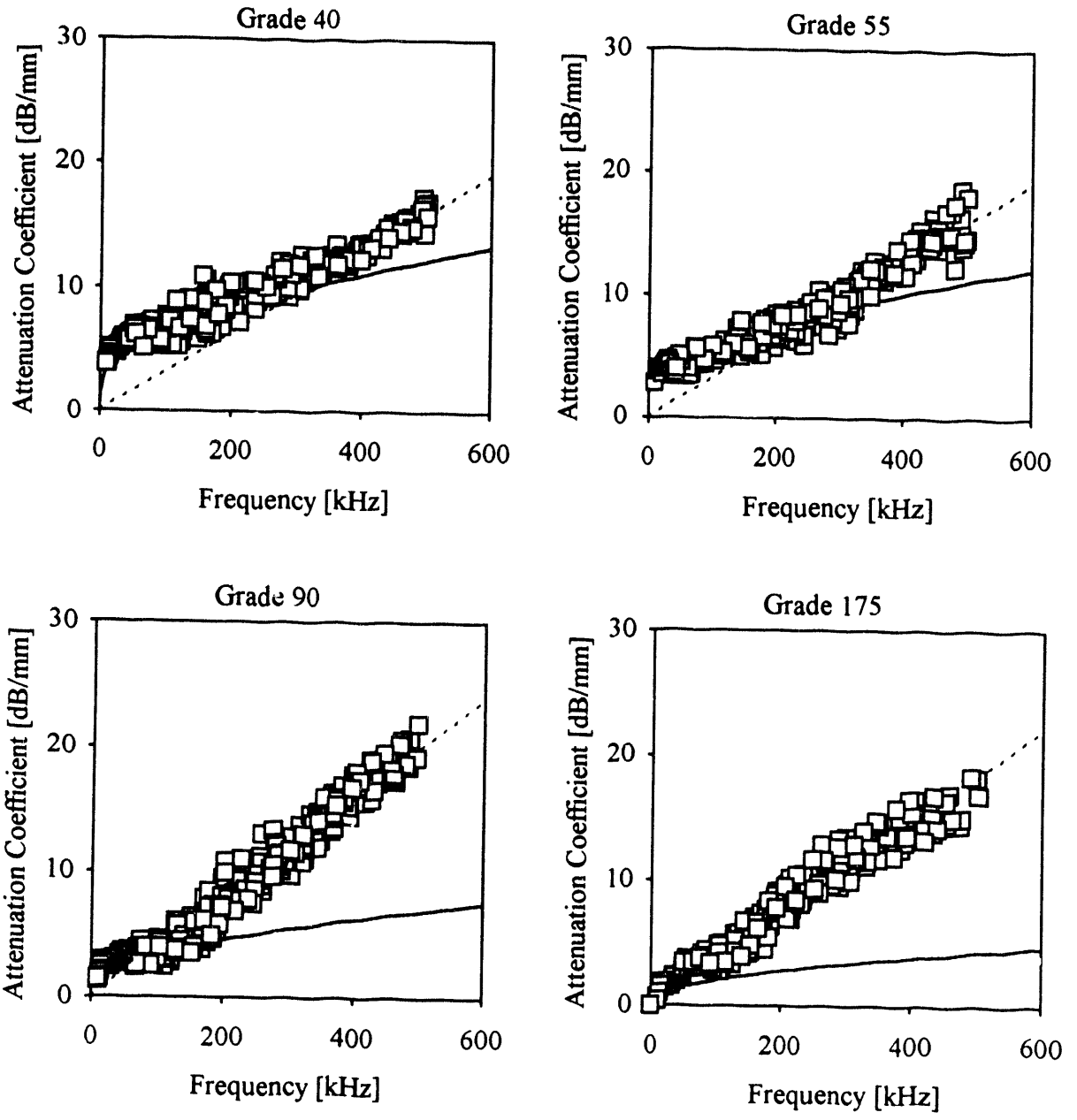

Figure 4 Comparison between the theoretically predicted (solid lines) and experimentally measured (square symbols) slow wave attenuations in cemented glass bead specimens for four different grades (high-frequency linear asymptotes are shown with dashed lines).

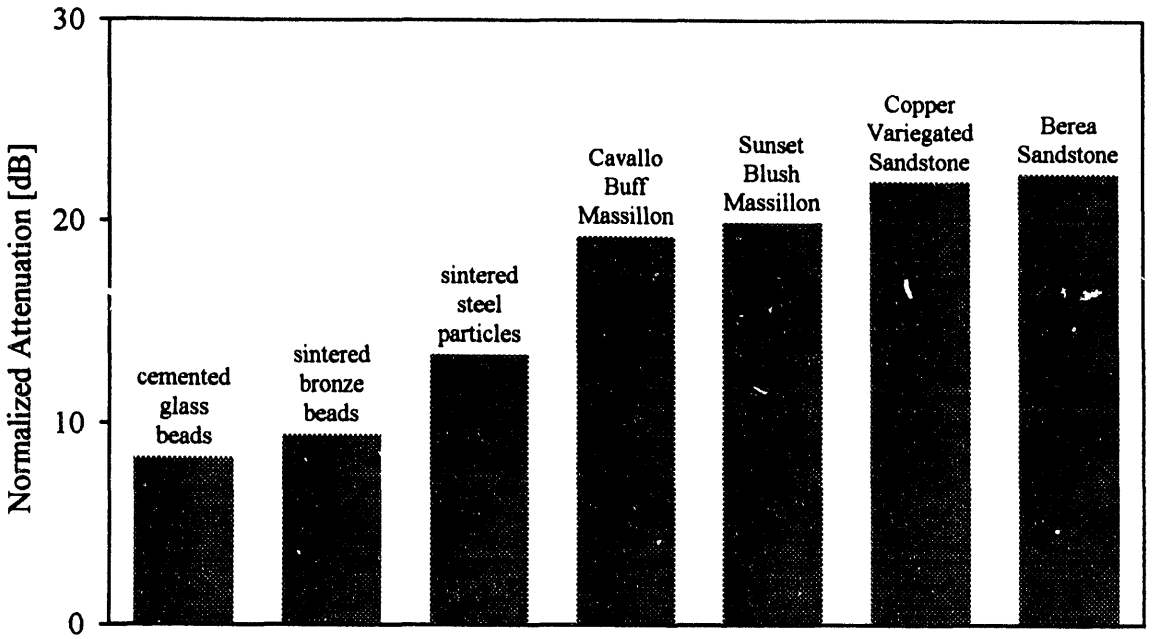

Figure 5 High-frequency limit of the normalized attenuation in a number of synthetic and natural rock materials.

attenuation only for Lorentzian phase distribution which is distinctly different from the theoretically predicted and experimentally observed distributions.[20-22] For all realistic distributions the dispersion curve becomes Gaussian provided the sample length is sufficiently large compared to the hydrodynamic correlation length. On the other hand, for a Gaussian phase distribution, the scattering induced loss is always proportional to the square of frequency.[23]

At this point, there seems to be no real evidence supporting Chaban's assumption that the phase distribution is Lorentzian. Actually, his calculations reveal the main problem with the concept of linearly frequency-dependent geometrical scattering, namely that it requires an apparently impossible phase perturbation of the acoustic wave. On the other hand, based on theoretical grounds only, elastic or geometrical scattering cannot be excluded as a possible explanation for the observed excess attenuation. Even without detailed calculations, we can postulate from the linear frequency dependence of the attenuation coefficient (constant normalized attenuation) that it has to be independent of the characteristic dimension of the

scatterer. This is because the dimensionality of the problem requires that the normalized attenuation be independent of the size of the scatterer when it is independent of the wavelength. This conclusion is at least not contradicted by our experimental results in the self-similar glass bead specimens, where the grain size changed almost one order of magnitude without any significant change in the high-frequency slope of the attenuation versus frequency curve. Of course, this apparent confirmation might be a pure coincidence and cannot prove by itself that the observed excess attenuation is caused by elastic or geometrical scattering. Actually, it would be rather unusual if the scattering induced attenuation turned out to be independent of the scatterer's size.

The excess attenuation could be also caused by viscous scattering, i. e., by increased viscous drag due to the rather uneven pore geometry or surface roughness. At very high frequencies, where the viscous skin depth δ is so much smaller than the pore radius a_p that it becomes comparable to the pore-wall surface roughness h, the viscous drag sharply increases and the attenuation of the slow compressional wave increases with frequency much faster than the expected square-root relation. This is because the peaks of the surface profile protrude into a region where the fluid velocity is already significant thereby greatly increasing the friction between the solid frame and the moving fluid column. In a recent study,[24] Gist showed that there is a transition frequency range where the normalized attenuation of the slow wave is roughly independent of frequency. Both below ($a_p \leq \delta$) and above ($\delta \leq h$) this transition range, the attenuation coefficient is proportional to the square-root of frequency. In the transition frequency range ($h \leq \delta \leq a_p$), the flow-pattern of the fluid is determined by the pore geometry, but the viscous friction is greatly increased by surface roughness. Although such conditions are more typical for water-saturation, the same effect might contribute to the observed excess attenuation in air-filled materials, too. For example, Waetzmann and Wenke found more than 50 years ago that the attenuation coefficient of airborne guided waves in ducts with rough walls deviates from the theoretically predicted square-root frequency-dependence and the excess attenuation is linearly proportional to frequency.[25]

As we have mentioned above, in the low-frequency diffuse regime, the normalized attenuation is constant at approximately 57 dB. At the transition between the diffuse and propagating regimes, the normalized attenuation starts to decrease and approaches an inverse square-root frequency dependence. For pores with smooth walls, this frequency-dependence is maintained up to very high frequencies where scattering becomes dominant. For pores with rough walls, the normalized attenuation does not decrease below a threshold value set by the surface roughness-to-pore size ratio. At very high frequencies, where the viscous skin depth becomes

negligible to the surface roughness, the normalized attenuation again assumes an inverse square-root frequency-dependence, but, at that point, scattering losses are obviously very high, too. In air-saturated specimens, there is not a wide window for more or less attenuation-free, dispersion-free slow wave propagation and the normalized attenuation can not significantly drop before scattering losses start to dominate. Consequently, the relative role of the surface roughness induced excess attenuation is much higher in water-saturated samples than in air-saturated ones. In air-saturated samples, the excess viscous attenuation caused by surface roughness and other pore shape irregularities is more difficult to separate from elastic and geometrical scattering losses which also start to give significant contributions to the observed total attenuation immediately above the diffuse regime. For example, in order to explain the 8.3 dB normalized attenuation observed in air-saturated glass bead specimens, we would have to assume that the surface roughness-to-pore diameter ratio is on the order of 10 %. This ratio is quite realistic considering the shape of the pores but is clearly beyond the validity of the simple approximations used to evaluate the excess viscous loss and the irregularity of the pore channel cannot be described simply as surface roughness.[26] Obviously, further analytical efforts are needed to develop appropriate models for these attenuation mechanisms so that the measured data can be evaluated in terms of microscopic geometrical properties of the permeable formation. We have to conclude that both viscous and elastic scattering mechanisms can explain the available experimental data and new conceptually different measurements are needed to obtain unequivocal evidence for the physical nature of the observed excess attenuation of the slow compressional wave in air-filled porous specimens at high frequencies.

1.1.3 INCOHERENT TRANSMISSION

Probably the most basic difference between viscous and elastic scattering is exhibited through their substantially different effect on the total acoustic energy carried by the slow compressional field. Viscous losses directly reduce the total acoustic energy by dissipation into heat. On the other hand, elastic or geometrical scattering simply converts the well-collimated coherent acoustic wave into diffusely propagating incoherent wave without reducing the total acoustic energy. Because of this fundamental difference between viscous and elastic scattering, the two mechanisms can be best differentiated from the energy balance of the total acoustic field. Unfortunately, ordinary phase-sensitive acoustic sensors are rather difficult to use for energy measurements since their output is proportional to the average field over their finite aperture. This makes them ideal to measure the transmitted (or reflected) coherent component of the total field when the receiving aperture is large with respect to the acoustic wavelength, but not for the

incoherent components.

Generally, the total acoustic field $u = u(x,y,z)$ can be written as

$$u = u_c + u_i \,, \tag{2}$$

where the coherent component is simply the ensemble average of the field for a large number of statistically identical representations of the randomly inhomogeneous medium. For practical purposes, the ensemble average is often substituted simply by the spatial average of the field for a large area covering the whole inhomogeneous specimen

$$u_c = \langle u \rangle \,. \tag{3}$$

From Equations 2 and 3, the incoherent field can be determined as the deviation from the average field

$$u_i = u - \langle u \rangle \,. \tag{4}$$

Of course, the total acoustic energy can be also written as the sum of the coherent and incoherent contributions

$$\langle u^2 \rangle = \langle u_c^2 \rangle + \langle u_i^2 \rangle \,. \tag{5}$$

For a thin plate, the incident acoustic energy is either reflected, transmitted or dissipated (Δ) within the plate

$$u_{inc}^2 = u_{c,r}^2 + u_{i,r}^2 + u_{c,t}^2 + u_{i,t}^2 + \Delta \,. \tag{6}$$

In the previously described insertion loss experiment, we actually measure only the coherent transmitted signal, $u_{c,t}$. By using a very small "point" sensor to map the field distribution just behind the porous plate, we could also measure the total transmitted field, $u_{c,t} + u_{i,t}$. More realistically, by using a sharply focused detector we can measure a combination of the coherent and incoherent field, $u_{c,t} + \gamma\, u_{i,t}$, where γ represents the forward scattered incoherent energy which falls within the angle of acceptance of the focused receiver. For example, assuming that a 1"-diameter beam is focused to a focal length of 1", the solid angle of acceptance for the receiver

is $\theta_{rec} \approx 0.84$ srad. In the simple case of unipolar scattering, this receiver would pick up approximately 7% of the total incoherent field (14% of the forward scattered "transmitted" incoherent wave). Naturally, in the case of dominantly forward directed scattering, an even larger fraction of the incoherent field can be accumulated to the receiver by such a simple focusing scheme and γ can be well over 14%. We shall demonstrate below, that even a very modest sensitivity of $\gamma \approx 1\%$ to the incoherent field would necessarily result in very strong incoherent detection if the observed excess attenuation were dominated by elastic or geometrical scattering. Naturally, in the case of viscous scattering the total field is attenuated almost as much as the coherent component since the missing acoustic energy is dissipated into heat. Even in the case of viscous loss, there will be a perceivable incoherent field because of the unevenness of the transmitted field caused by the inhomogeneity of the material, but the incoherent transmission will be of the same order of magnitude (i. e., within a few dB) as the coherent transmission. In contrast with elastic and geometrical scattering, the source of this incoherent field is the uneven distribution of the dissipative loss. This is why we use the term of viscous scattering when a significant, but not dominating, incoherent component is generated. Of course, in the case of a completely homogeneous viscous medium (e. g., a rubber plate) the missing coherent energy is fully converted into heat and there is no incoherent scattering at all.

In order to determine whether the missing energy of the coherent transmission indicated by the observed excess attenuation is primarily viscous loss or rather incoherent elastic and geometrical scattering, we modified our experimental arrangement. Our original system used large-aperture unfocused transducers and measured only the coherent transmission. The modified system is shown in Figure 6. The most important difference is that the receiver is equipped with a 1"-focal-length Plexiglas lens which assures a small receiving aperture of approximately 1 mm in diameter at 250 kHz. In this way we can map the distribution of the total transmitted field without blurring the local deviations from the average wave. Because of the excessive time averaging needed to eliminate electrical noise, a single measurement took approximately one minute with our previous system. This relatively sluggish operation was acceptable in the case of strictly coherent measurements since the unfocused transducer inherently averages over a 1"-diameter area of the specimen and larger areas can be covered in a few steps. Much faster operation is desirable in the case of point-by-point mapping of the total transmitted field, since it takes more than 500 individual measurements, i. e., more than eight hours with our original system, at a scanning resolution of 1 mm to cover the 1"-diameter spot seen by the unfocused transducer in a single measurement. In order to facilitate faster measurements, we replaced the external digital oscilloscope with a high-speed on-board digital-to-analog converter. This allowed us to increase the speed of data acquisition by roughly one order of magnitude. At the same time, we also

replaced the external function generator by a digital waveform synthesizer plugged into the computer. This modification allowed us to control the carrier frequency, length and amplitude of the tone-burst by software means and therefore to further automate our system. These improvements enabled us to increase our dynamic range to 90 dB without sacrificing the speed of data acquisition. The specimen is mounted on a computer controlled translation stage for automated scanning. Later we shall demonstrate that these modifications made it possible to use our experimental system as a high-sensitivity, high-resolution slow wave imaging device, a major new application for the air-saturated ultrasonic inspection technique.

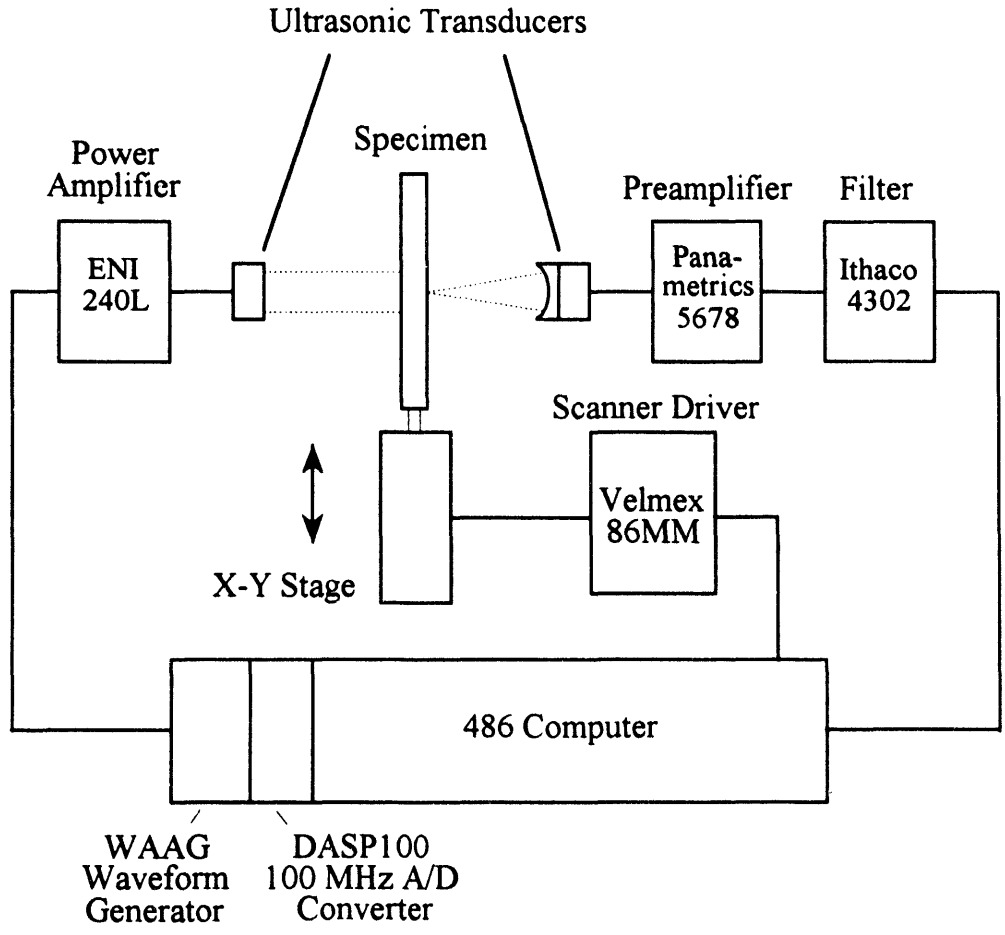

Figure 6 Block diagram of the modified experimental system.

Figure 7 shows the point-by-point insertion loss and insertion delay distribution through a 3.2-mm-thick cemented glass bead specimen of Grade 175 at 250 kHz. This particular specimen was used in this part of the study because, although all other inspected specimens showed

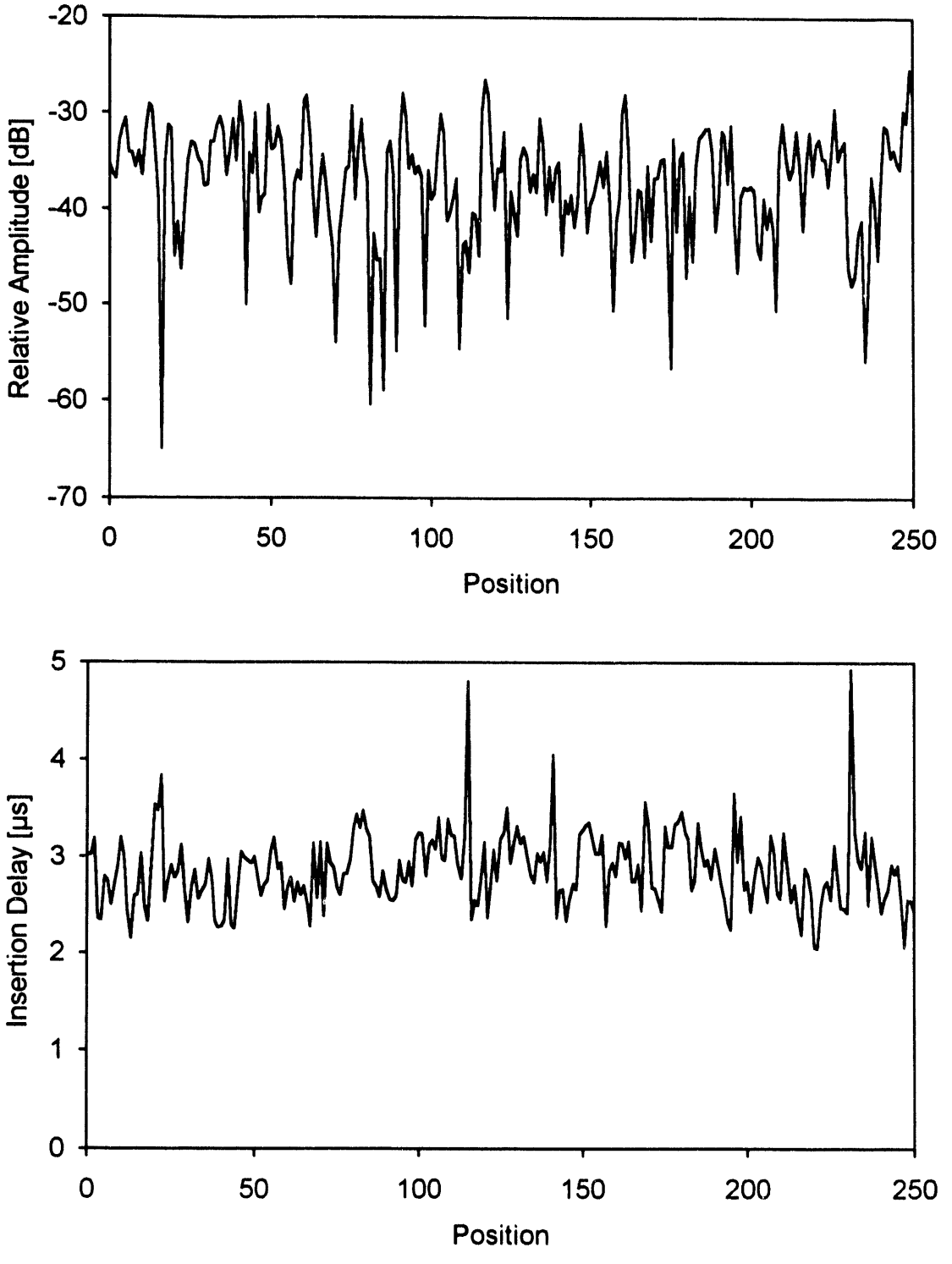

Figure 7 Point-by-point insertion loss and insertion delay distribution through a 3.2-mm-thick cemented glass bead specimen of Grade 175 at 250 kHz.

evidence of anomalous attenuation at high frequencies, this sample exhibited by far the strongest excess attenuation. Our coherent measurements indicated approximately 10 dB/mm attenuation at 250 kHz, more than three times the 3 dB/mm viscous loss predicted by Attenborough's model (see Figure 4). According to Figure 7, both insertion loss and delay reveal the presence of significant incoherent components in the transmitted field. Figure 8 shows the probability densities of the insertion loss and time distributions as well as the cross-correlation between these two parameters. The insertion loss and delay are obviously not entirely independent of each other in a statistical sense. As one would expect, propagation along longer, more tortuous pore channels is more attenuated, but the correlation is not very strong. The average intensity of the total transmitted field $< u_t^2(x,y) >$ is 36 dB below the incident field. The total field is the sum of the coherent and incoherent components. The amplitude $u_t(x,y)$ and phase $\varphi(x,y)$ of the total transmitted field can be directly calculated from the measured insertion loss $L_i(x,y)$ and delay $T_i(x,y)$ as follows

$$u_t(x,y) = u_{inc}\, 10^{-L_i(x,y)/20} \tag{7}$$

and

$$\varphi(x,y) = 2\pi f\, T_i(x,y), \tag{8}$$

where f is the ultrasonic frequency. The coherent component is then

$$u_{c,t} = < u_t(x,y) e^{i\varphi(x,y)} > \tag{9}$$

and the incoherent field is

$$u_{i,t} = u_t(x,y) - < u_t(x,y) e^{i\varphi(x,y)} > . \tag{10}$$

From Equations 9 and 10, the coherent and incoherent transmitted powers are $u_{c,t}^2 = -38.9\,\text{dB}$ and $< u_{i,t}^2 > = -38.5\,\text{dB}$, respectively. In other word, there is a perceivable incoherent component, but not significantly stronger than the coherent one, even when considering the possible underestimation in the transmitted incoherent field described before. We know that out of the measured ≈39 dB coherent loss, app. 5 dB is due to coherent reflection from the plate caused by impedance mismatch.[14] Furthermore, only less than 10 dB viscous loss is accounted for by Attenborough's analytical model therefore as much as 24 dB excess attenuation occurred.

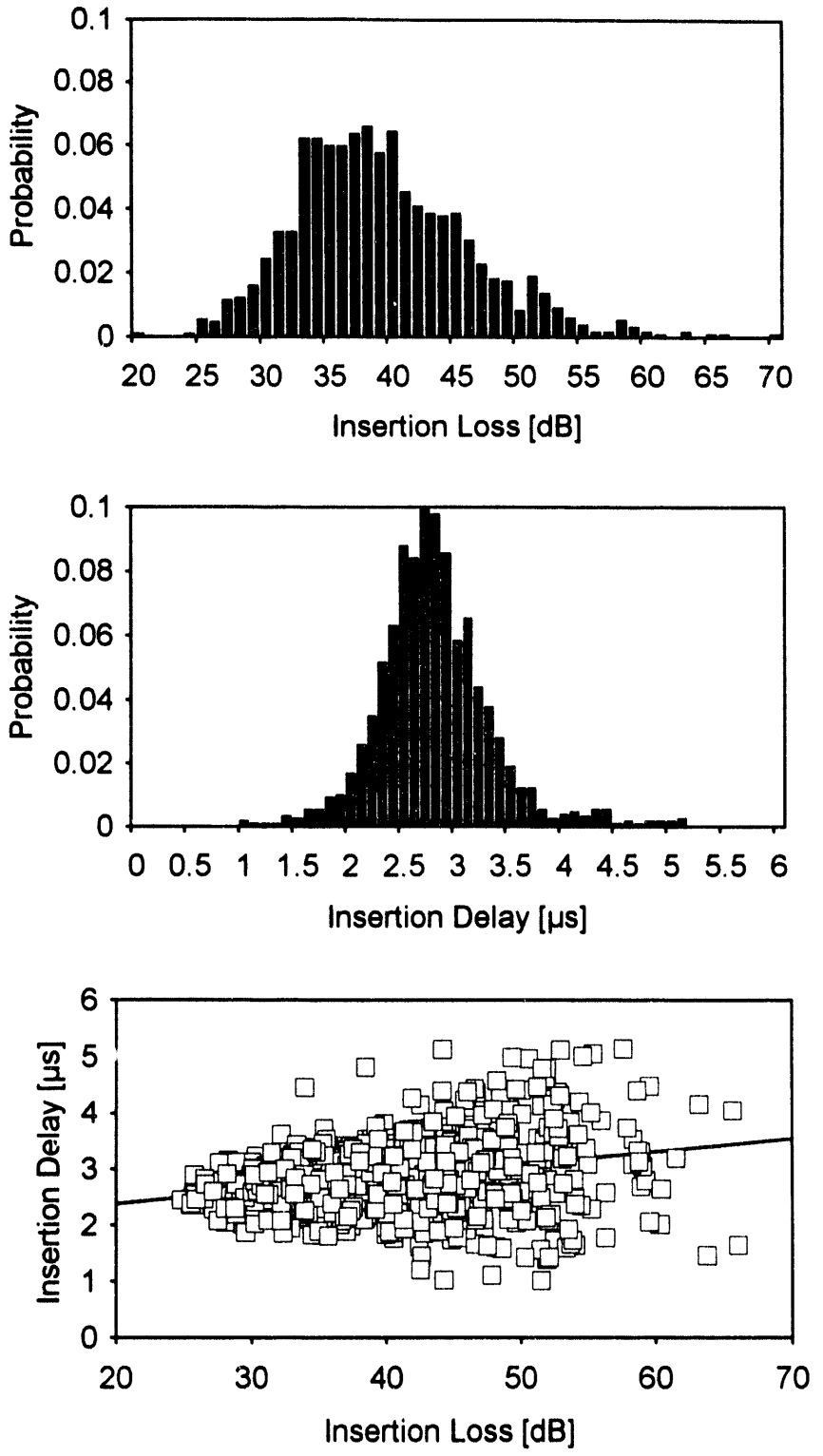

Figure 8 Probability densities of the insertion loss and time distributions and the cross-correlation between these two parameters.

Assuming that only elastic and geometrical scattering is responsible for this excess attenuation, and that this scattering is unipolar, i. e., evenly distributed in every direction, the forward scattered (transmitted) part of the incoherent wave should be only 5 + 10 + 3 = 18 dB below the incident field. Our measurements revealed only roughly 1% of this incoherent energy, which seem to strongly indicate that most of the energy missing from the coherent transmission is not converted into incoherent acoustic scattering but dissipated into heat. If elastic or geometrical scattering dominated the observed excess attenuation the field would be strong but very irregular behind the plate. These measurements show that the field becomes generally very weak behind the plate, which suggests that the loss is dominantly due to viscous scattering.

The same general conclusion can be drawn from a number of other observations, too. For example, The probability density of the insertion delay distribution shown in Figure 8 is essentially Gaussian with a standard deviation of 0.4 μs. The corresponding $\varphi_{rms} \approx 36^{o}$ root-mean-square phase modulation is too small to indicate geometrical scattering on the order of the observed excess attenuation. The loss of the coherent signal due to geometrical scattering can be calculated in the phase-screen approximation[23] as $\frac{1}{2}\varphi_{rms}^{2}$ which is less than 2 dB. Again, it appears that the total field become not so much uneven as generally weak. Another way to differentiate between viscous and elastic scattering is by considering the frequency dependence of the total field at any particular point. In the case of viscous scattering, a darker than average point remains dark at all frequencies as the signal becomes progressively weaker with increasing frequency. In comparison, in the case of elastic or geometrical scattering, a dark spot is generally due to destructive interference between otherwise strong incoherent components. The same spot often becomes brighter at higher frequencies, a clear sign of dominantly incoherent transmission, which cannot happen in the case of viscous scattering. Figure 9 shows the point-by-point comparison between the measured insertion loss at 240, 280, and 320 kHz in the same cemented glass bead plate. There is a generally strong but less than perfect correlation between the measured losses at different frequencies. From the linear frequency dependence of the coherent attenuation, the insertion loss is expected to be 16.7% lower at 240 kHz than at 280 kHz. The point-by-point statistical analysis indicated a difference of 16.2 ± 1.4%. Similarly, the insertion loss is expected to be 14.3% higher at 320 kHz than at 240 kHz. The point-by-point statistical analysis indicated a difference of 12 ± 2%. In other words, the unevenness of the total transmitted field is primarily due to the presence of highly transparent and strongly attenuating regions instead of random interference caused by strong incoherent waves. This also indicates that the observed excess attenuation is primarily due to viscous scattering with some evidence of much weaker elastic and geometrical scattering.

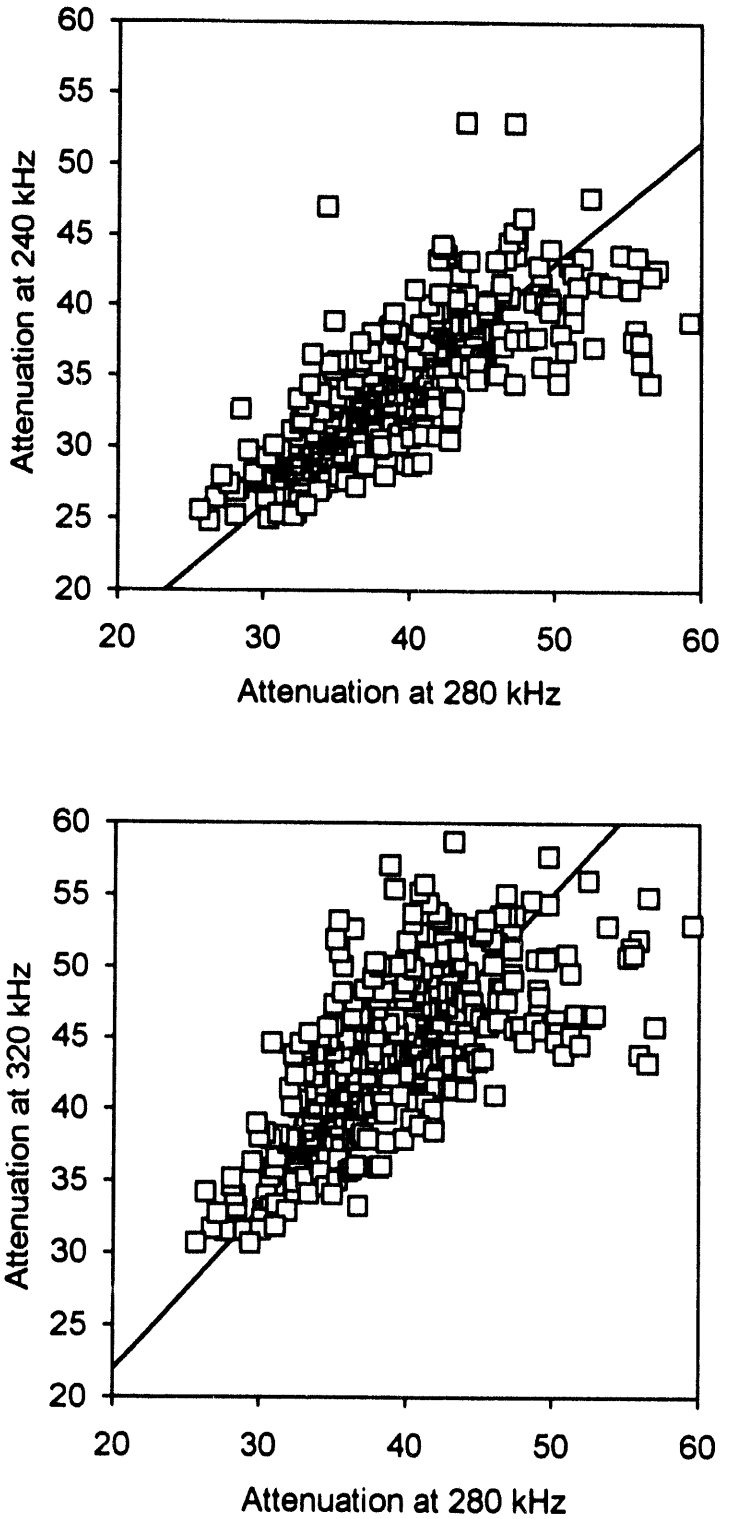

Figure 9 Point-by-point comparison between the measured insertion loss at 240, 280, and 320 kHz in the same cemented glass bead plate.

The same effect can be observed on the two-dimensional maps of the transmitted acoustic wave shown in Figure 10 for three different frequencies. All three pictures were taken from the same 2" x 1.4" area. Since the average attenuation increases from less than 30 dB at 210 kHz to more than 50 dB at 380 kHz, each picture was normalized to the average loss at that particular frequency. The total dynamic range of the pictures from black to white was limited to 30 dB with 16 gray levels. There is an apparent increase in both contrast and resolution with increasing frequency, but a detailed comparison reveals that areas of darker or brighter intensity remain darker and brighter, respectively, at all frequencies. These pictures well illustrate that in spite of the presence of some incoherent components caused by elastic and geometrical scattering, the dominating loss mechanism is viscous scattering.

Similar experiments were conducted in a number of other synthetic and natural rocks. In each case, we found perceivable signs of elastic and geometrical scattering but the dominating loss mechanism appeared to be of viscous nature. In an effort to verify the feasibility of distinguishing between geometrical and viscous loss by analyzing the incoherent content of the transmitted acoustical field, we prepared a cemented glass bead specimen from huge, 6-mm-diameter spheres. Since the geometrical scattering increases while viscous losses decrease with increasing grain size, the first has to become the dominant loss mechanism for very large beads. We found that in this specimen the incoherent intensity was more than a 100 times higher than the coherent one and the observed attenuation of the coherent signal was actually due to the randomness or incoherence of the field rather than to the lack of transmitted energy. In all other samples with grain sizes around 1 mm or less the observed excess attenuation appears to be of viscous nature.

210 kHz

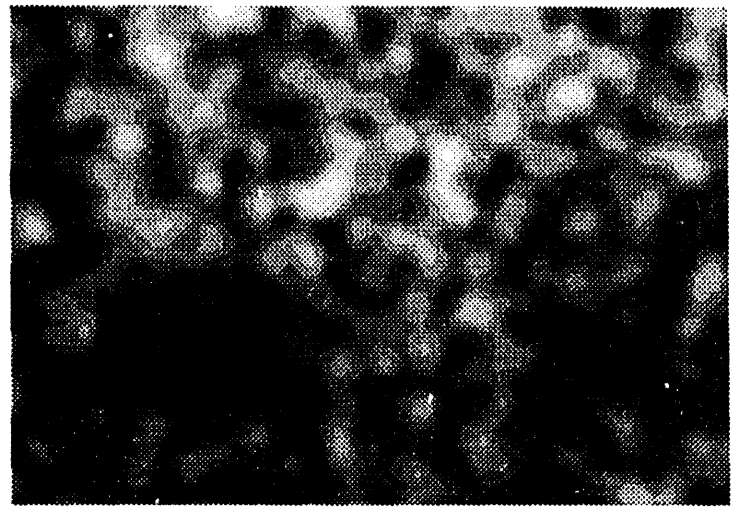

290 kHz

380 kHz

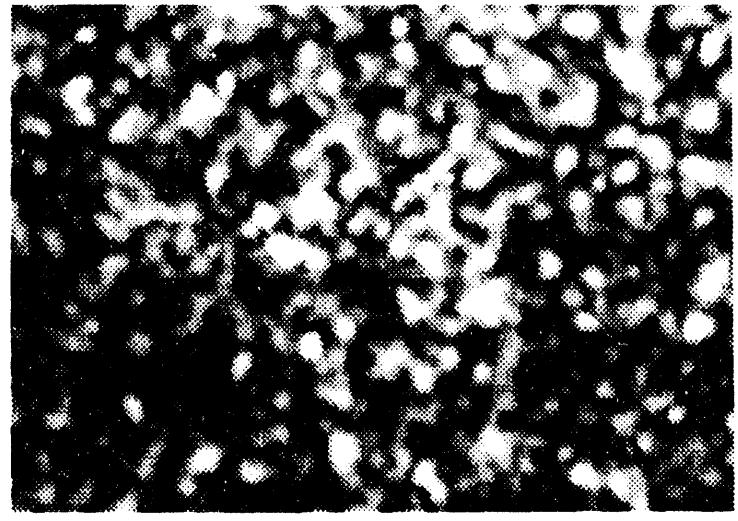

Figure 10 Transmission images of a Grade 175 glass plate at three different frequencies.

1.1.4 CONCLUSIONS

Transmission of airborne ultrasonic waves through thin air-filled porous plates was used to study slow wave propagation in permeable solids. We used Attenborough's theoretical model to fit the experimental data and found good agreement except at high frequencies where scattering losses dominated the attenuation of the slow wave. This discrepancy has been expected since, for air saturation, there is no frequency "window" where both viscous and scattering losses are weak simultaneously. Due to the excellent sensitivity of the suggested experimental technique, low-permeability materials including natural rocks can be inspected, too. Currently, the threshold sensitivity of our system is approximately 100 mD. Further improvements can be expected from reflection-type measurements to be discussed later in the following proposal.

We have further developed or experimental system by introducing focused inspection. The primary purpose of this modification was to study the incoherent components in the transmitted acoustic wave in order to identify the physical mechanism of the previously observed excess attenuation at high frequencies. Our measurements indicate that the excess attenuation is mainly due to increased viscous losses. The irregularly shaped pore channels and the macroscopic inhomogeneity of the porous frame results in a highly uneven flow pattern which increases the viscous losses and effectively decreases the dynamic permeability of the material. Further analytical efforts are needed to develop appropriate models for these attenuation mechanisms so that the measured data can be evaluated in terms of geometrical properties of the permeable formation.

Our current research effort is directed at studying the physical nature of the previously observed anomalous high-frequency attenuation of the slow compressional wave in air-filled porous materials. To achieve this goal we adapted our experimental system to mapping the spatial distribution of the partially incoherent transmitted wave. An important spin-off of the necessary technical improvements such as beam focusing, automated scanning, increased dynamic range, greatly accelerated data acquisition, etc., is the development of a new slow wave imaging concept which can be used to study the inhomogeneous pore structure in a permeable solid. In the following proposal, we shall suggest further technical improvements and specific scientific problems to be investigated to develop a new slow wave imaging technique to characterize rocks and other permeable solids.

1.2 SURFACE WAVE TECHNIQUE

As we have mentioned before, the bulk slow wave propagating in a water-saturated natural rock is usually far too weak to be detected, let alone to be used for materials characterization. On the other hand, surface and interface waves guided along the contour of a water-saturated specimen are much less attenuated but still quite sensitive to the permeable nature of the porous formation. Maybe the best example is a borehole Stoneley wave which is the fundamental mode of a guided wave traveling in a fluid-filled tube. In the case of permeable walls, because of fluid flow into the formation, the Stoneley wave velocity decreases and its attenuation increases. The strong correlation between the frequency-dependent propagation parameters and formation permeability can be exploited in acoustic logging in the field or in the laboratory.[27-31] It has been suggested that other types of guided modes can be also used in a similar way to assess formation permeability, tortuosity, and other parameters of a porous material.[32-37]

1.2.1 INTRODUCTION AND BACKGROUND

There is only one type of true interface wave which can propagate along the free surface of an ordinary solid. It is called Rayleigh wave and its velocity is approximately 5-10% below the shear wave velocity. Two types of interface waves can propagate along the fluid-loaded surface of an immersed ordinary solid: there is a true mode called Stoneley (or sometimes Scholte) wave and a pseudo-mode called leaky Rayleigh wave. The true wave is always slower than all the bulk waves in the solid and the fluid and it produces evanescent fields only as it propagates along the interface. Since the energy of this mode is strictly confined to the interface region, its generation and detection presents a rather difficult technical problem. The leaky Rayleigh wave is slightly faster than the true Rayleigh wave propagating on the free surface of a solid. In most cases, this velocity is faster than the sound velocity in the fluid, therefore it leaks energy into the liquid as it propagates along the interface. This mode can be easily generated and detected by the phase-matching compressional wave in the fluid at the so-called Rayleigh angle, at least whenever this angle is not much higher than 60^{o}. It should be mentioned that this mode becomes non-propagating whenever the shear velocity in the solid is lower than the sound velocity in the fluid, which is true for many natural rocks.

Acoustic wave interaction with a plane interface separating a superstrate fluid and a fluid-saturated porous solid substrate is governed by four boundary conditions.[38] Three of them,

namely the continuity of normal stress and displacement and the disappearance of the transverse stress at the interface, are the usual conditions required at ordinary fluid/solid interfaces. The only conceptual difference in the case of permeable solids is that the continuity of the normal displacement has to be modified to express the conservation of fluid volume:

$$U_n' = \phi U_n + (1-\phi) u_n, \tag{11}$$

where U_n', U_n, and u_n are the normal displacement components of the superstrate fluid, and the substrate fluid and solid, respectively, and ϕ denotes the porosity. The fourth boundary condition is Darcy's law applied to the surface pores of the permeable solid. The surface impedance Z_s is defined as the ratio between the discontinuity in pressure and the relative volume velocity of the fluid with respect to the frame below the interface:[27,38]

$$p - p' = i\omega Z_s \phi (U_n - u_n) \tag{12}$$

where p and p' denote the fluid pressure in the pore space below the surface and in the superstrate fluid just above it, respectively, and ω is the angular frequency. Generally, Z_s is complex and the definition of Equation 12 has to be used. In the case of a fluid/fluid-saturated porous solid interface (e.g., in borehole Stoneley wave experiments), the finite surface impedance is due to the flow resistivity of the surface pores and its value depends on the viscosity of the fluid. We have recently suggested that, due to surface tension, practically closed-pore boundary conditions can prevail at an interface between a non-wetting fluid (e. g., air) and a porous solid saturated with a wetting fluid (e. g., water).[37] In this case, the surface impedance is very high because of the stiffness of the microscopic fluid membranes extended by capillary forces over the otherwise open surface pores. Since the surface impedance is pure imaginary, it is advantageous to introduce a surface stiffness parameter $T_s = i\omega Z_s$ so that the discontinuity in pressure is proportional to the average surface displacement of the fluid[32,33]

$$p - p' = T_s \phi (U_n - u_n). \tag{13}$$

In the case of ordinary solids, the previously mentioned three boundary conditions can be satisfied by three bulk waves, namely the reflected compressional wave in the fluid and the longitudinal and shear transmitted waves in the solid. In the case of a permeable solid, an additional boundary condition is necessary to account for the presence of a fourth component, i. e., the slow compressional wave in the fluid-saturated solid.

Naturally, the most obvious effect of the increasing surface impedance is the sharp decrease in the transmitted slow compressional wave.[39] Interestingly, surface modes propagating along the interface are even more crucially dependent on the surface impedance. Ten years ago, Feng and Johnson predicted the presence of a new slow surface mode on a fluid/fluid-saturated porous solid interface with closed surface pores.[32,33] They showed that a maximum of three different types of surface modes can exist on a fluid/fluid-saturated porous solid interface depending on (i) the shear velocity of the frame and (ii) the surface conditions, i.e., whether the pores are open or closed. However, in most natural rocks the shear velocity is lower than the sound velocity in water and the pores are open at the surface, therefore there is but one principal surface mode, namely the Stoneley mode. It is important to realize that this mode becomes leaky into the slow compressional wave whenever its velocity is higher, as it is in most cases of interest to us. Although the slow wave is very highly attenuated and cannot be directly observed in water-saturated rocks, its indirect effect of making the Stoneley wave highly attenuated via this leakage can be more readily observed. This attenuation mechanism is taken advantage of for permeability assessment in the Stoneley borehole technique. Of course, in the case of an impermeable ordinary solid, the Stoneley wave is a true interface wave with lower velocity than any of the bulk velocities in the surrounding media.

In fully immersed porous materials, the slow interface wave cannot be observed, unless the surface pores are artificially closed somehow. The corresponding slow surface wave propagating along the free surface of a fluid-saturated porous solid seems to be easier to observe experimentally because the pores, which are naturally open when fully submerged in a wetting fluid, are essentially closed by capillary forces.[37] In the ideal case of completely closed surface pores and viscosity-free fluid, two types of surface wave can propagate: there is a pseudo-Rayleigh mode, which leaks its energy into the slow compressional wave, and a "true" surface mode with velocity slightly below that of the slow wave. The second mode is a simple form of the new interface mode predicted by Feng and Johnson when the superstrate fluid is extremely rare and highly compressible like air (theoretically, the slow interface mode becomes slightly leaky, too, since its velocity is higher than the sound velocity in air, although the actual energy loss is negligible because of the large density difference between the two fluids).

The effect of completely "open" ($T_S = 0$) and completely "closed" ($T_S = \infty$) surface pores on the interaction of an acoustic wave with the fluid/fluid-saturated porous solid interface is quite easy to understand, but intermediate cases are much more complicated. A question of great practical importance is where and how the transition between these limiting cases occurs. Figure

11 shows the calculated velocity of the "true" slow surface wave and the leaky Rayleigh wave propagating on the surface of water-saturated porous glass as functions of the surface stiffness. The following parameters were used in these calculations (with the notation of Ref. 32): $\rho_f = 10^3$ kg/m^3, $\rho_f' = 1.3$ kg/m^3, $\rho_s = 2.48\ 10^3$ kg/m^3, $K_f = 2.25\ 10^9$ N/m^2, $K_f' = 1.5\ 10^5$ N/m^2, $K_s = 4.99\ 10^{10}$ N/m^2, $K_b = 6.64\ 10^9$, $N = 3.69\ 10^9$ N/m^2, $\phi = .38$, $\alpha = 1.79$. The "true" slow surface wave appears only above $T_s \approx 10^7$ N/m^3 where its velocity is equal to the slow bulk velocity. The velocity of this mode slightly decreases with increasing surface stiffness, but it flattens off above $T_s = 10^8$ N/m^3, and the total change is only approximately 5 %. The Rayleigh velocity slightly increases as the surface stiffness increases and the transition is also around $T_s = 10^7$ N/m^3. It should be mentioned that Wu et al. obtained roughly the same transition value for the surface stiffness between open- and closed-pore boundary conditions by analyzing the reflection coefficient of a water/water-saturated porous glass interface at normal incidence.[13]

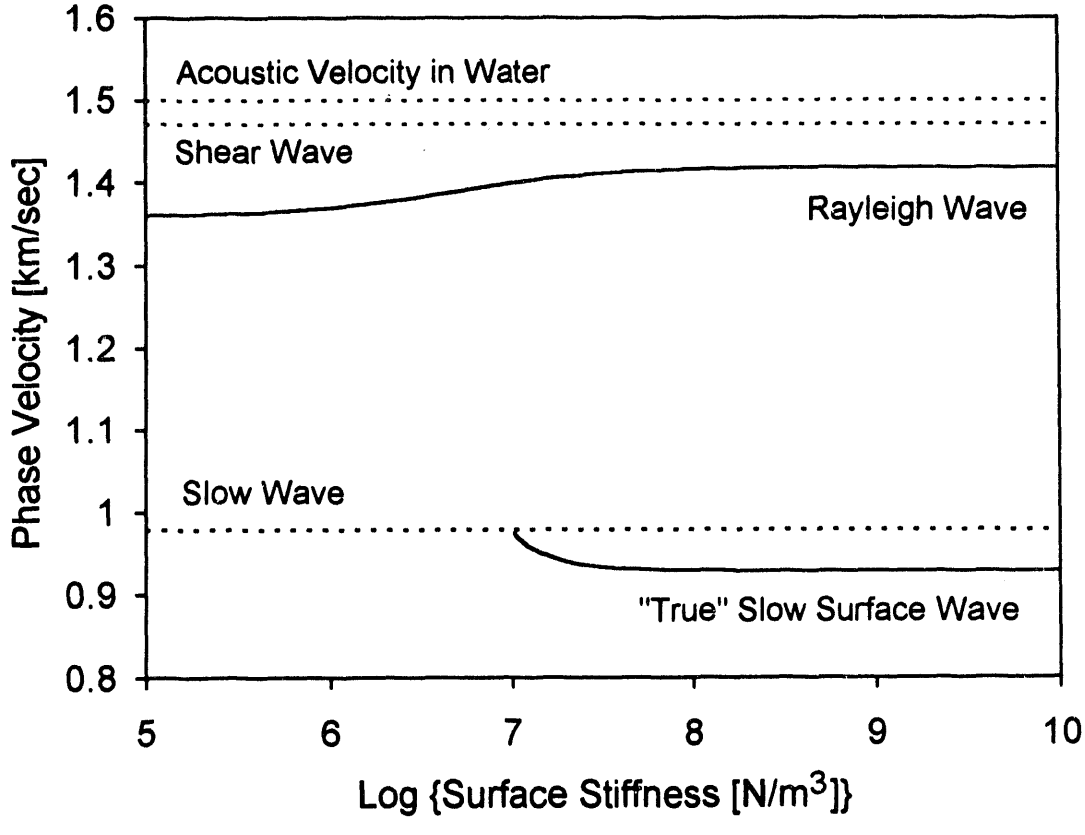

Figure 11 Surface wave velocity versus surface stiffness on the free surface of water-saturated porous glass.

Our preliminary results based on conventional contact transducer measurements indicated that the surface stiffness threshold required for slow surface wave propagation is usually exceeded by the surface membrane in porous solids of 10,000 mD or lower static permeability. As a result, a highly attenuated slow surface mode can be observed unless the permeability is less than 100 mD and the viscous loss becomes excessive.[40] Figure 12 shows the measured surface wave velocity in water-saturated Massillon and Berea sandstones between 100 and 600 mD at 100 kHz. In natural rocks, as long as two-to-five days are necessary to achieve full saturation with water at room temperature. The shear velocity is basically unaffected by water saturation, although it drops 2-3% as a result of the added inertia of the liquid. In comparison, in the most permeable rocks, the surface wave velocity drops as much as 40 % due to the presence of the slow surface mode. In low-permeability samples, below approximately 200 mD, the fluid is essentially immobilized in the pores by viscous forces. Such rocks behave like ordinary solids; the surface wave velocity is only a few percent lower than the shear velocity regardless whether the sample is saturated or not. In the next chapter we present our new experimental results on improved laser interferometric observation of the slow surface mode and an improved theoretical approach used to interpret the experimental data. In the subsequent chapter we describe our efforts directed at the independent experimental verification of the assumed closed-pore boundary condition by direct acoustic measurement of the quasi-static surface stiffness of fluid saturated porous solids.

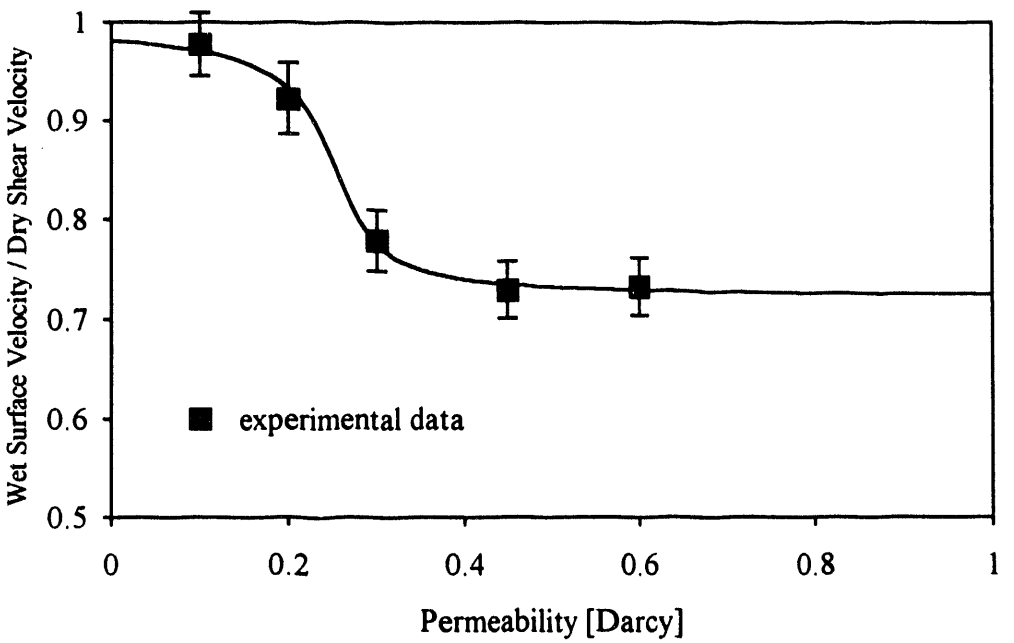

Figure 11 Normalized surface wave velocity versus permeability in wet sandstones.

1.2.2 LASER INTERFEROMETRIC OBSERVATION OF THE SLOW SURFACE WAVE

In spite of its obvious advantages over conventional contact and immersion techniques, laser interferometry has not yet become a practical tool in ultrasonic materials characterization since its sensitivity is insufficient in most practical applications. Part of the problem is that the maximum signal-to-noise ratio often cited in scientific publications and manufacturers' specifications cannot be maintained on ordinary diffusely reflecting surfaces. Although these surfaces reflect a fair amount (5-50%) of the incident laser light, this energy is randomly distributed among a large number of bright speckles. When using coherent laser light to irradiate rough surfaces such as that of a natural rock, the image of the illuminated object exhibits a random interference modulation, or "speckle pattern". Phase cancellation caused by the random phase distribution of these speckles means that averaging more than one speckle over the detector's aperture does not increase the interferometric signal. Unless the detector happens to see one of the bright speckles, the interferometer's signal-to-noise ratio will be much lower than the optimum. The available coherent optical reflection from a diffuse surface is limited by the total laser power contained in a single speckle. Even the limited sensitivity set by this restriction is quite difficult to realize in practice since it assumes that the photo diode is covered by a single bright speckle. Normally, the photo diode is only partially covered by a bright speckle and occasionally a completely dark speckle is encountered. Therefore, when scanning the surface of an object with a laser interferometer, the threshold sensitivity inherently fluctuates. Although the absolute sensitivity is the same everywhere, the detector's noise level greatly increases when darker speckles are encountered. At certain points, the reduction of the optical reflection may exceed the dynamic range of the electronic system and another nearby point must be chosen on the surface for detection. This inherent limitation of the conventional laser heterodyne interferometer effectively excludes any application on natural rocks or even on porous ceramics.

We have recently developed a novel interferometric method which eliminates the above described limitation of heterodyne interferometry on rough, diffusely scattering surfaces.[41,42] Keeping one bright speckle on the aperture of the photo diode all the time is nearly impossible, but it is feasible to assure that a bright speckle falls on the photo diode for some of the time by simple moving the speckle pattern around at an appropriate speed by means of a simple electro-mechanical modulator. For example, if there is only a 1 % chance of a very bright speckle's covering a detector, we can still choose a modulation amplitude and frequency that assures that approximately 100 bright speckles hit the photo diode per second and that the duration of these

flashes can be a few hundred microseconds, i. e., sufficiently long to trigger the transmitter and detect the ultrasonic pulses before the speckle moves away. This so-called random speckle modulation technique does not increase the peak sensitivity of the interferometer, which is acceptable in many materials characterization applications, but it maintains this peak sensitivity everywhere on a diffusely reflecting surface, which is absolutely necessary in our current application. In the conventional mode of operation, i. e., without the random speckle modulation, the focal range of the laser interferometer is less than 1 mm which requires that the object be placed precisely at the focal distance and be kept there within a few tenths of a millimeter. Even then, the interferometric signal might be very weak whenever a dark speckle is encountered accidentally. At these points, the signal-to-noise ratio might be so low that either the test object or the interferometer has to be moved a little to regain an acceptable signal. On the other hand, random speckle modulation completely eliminates these very dark speckles and extends the effective focal range to approximately 10 mm. The random speckle modulation technique greatly increases the average signal-to-noise ratio in the case of severely rough samples. Without it, some of the detected ultrasonic signals are completely lost in noise as the specimen is scanned to monitor the surface vibration during saturation. As a result of the random speckle modulation, the signal-to-noise ratio is equally high everywhere and very close to the best value that can be achieved by conventional interferometry from very smooth, specularly reflecting surfaces.

One of the most demanding applications for laser interferometry is ultrasonic measurements on ceramics and natural rocks. Even when we carefully polish these materials, the surface still remains somewhat rough because of the inherently coarse grain structure, and specular optical reflection cannot be assured unless some kind of coating is applied to the surface. The previously described random speckle modulation technique is especially well suited for the inspection of such naturally diffuse samples. Figure 12 shows the typical geometrical configuration used to measure surface wave velocity by optical detection. The surface wave is excited by a vertically polarized shear wave transducer mounted at the edge of the specimen. The normal component of the surface vibration is measured by the laser interferometer at at least two locations along the propagation path. Extensive time averaging is used to eliminate electrical noise. In addition, spatial averaging is used to reduce the variance of the signal due to the rather strong incoherent scattering in such coarse-grained materials. This is achieved simply by scanning the laser beam in the lateral direction during averaging. As an example, Figure 13 shows the detected signals at two different positions in a Buff Limestone specimen. The Rayleigh velocity can be readily calculated from the propagation delay as 2,270 m/s.

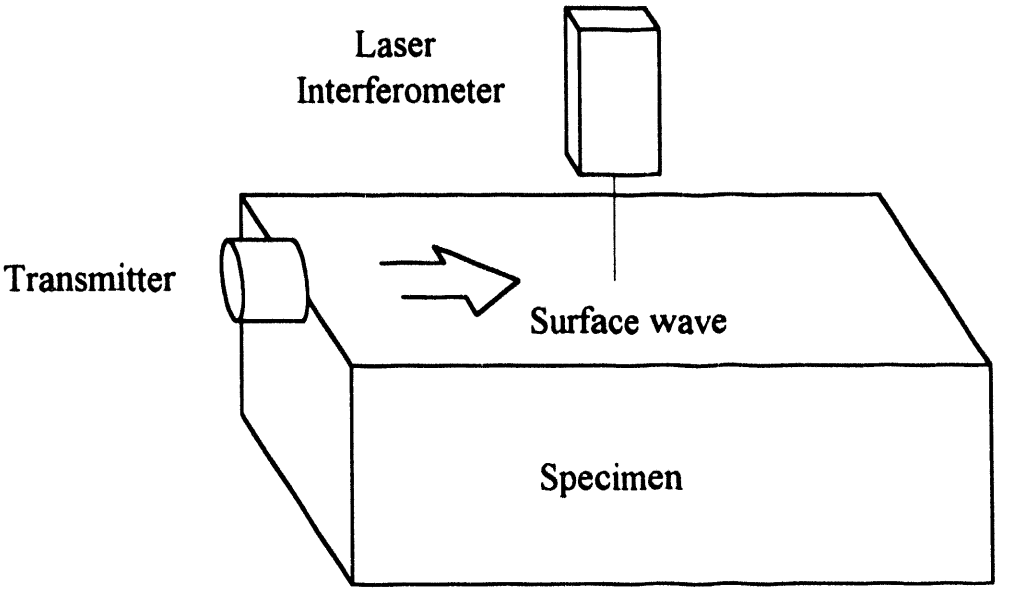

Figure 12 Experimental arrangement for surface wave measurements by laser interferometer.

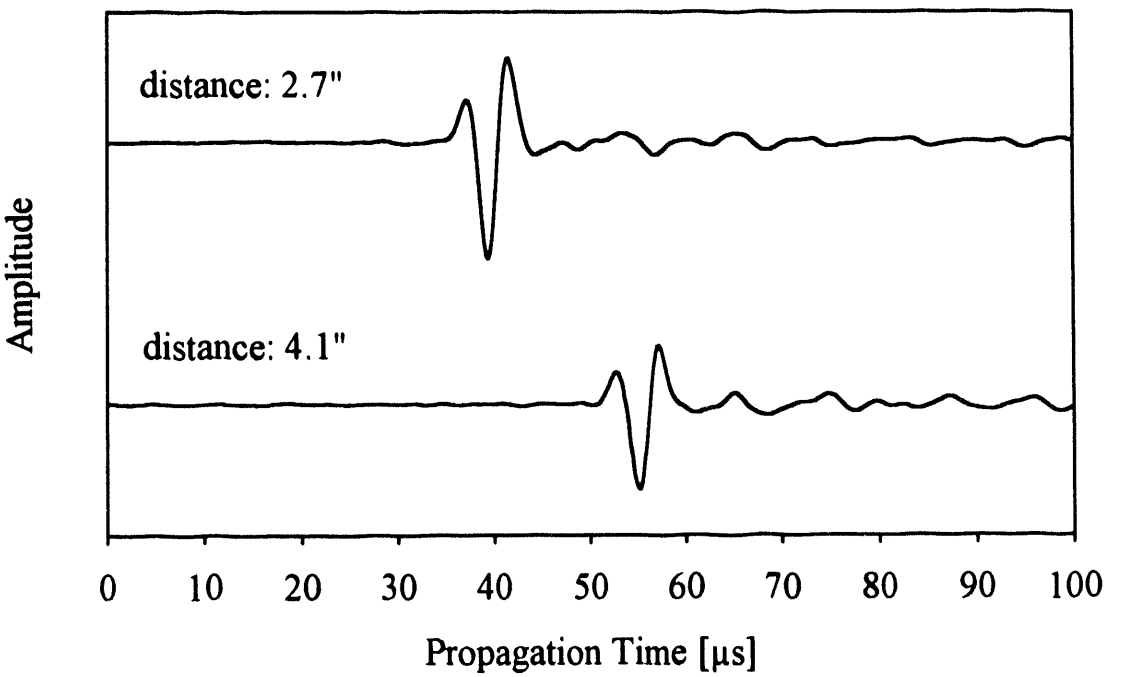

Figure 13 Optically detected surface vibration in Buff Limestone.

Thanks to the random speckle modulation technique, the sensitivity and reliability of the heterodyne interferometer is quite sufficient to conduct similar experiments even in highly attenuating samples of poor optical reflectivity. The same technique was recently used in the first successful experiment to observe the "slow" surface wave propagating on fluid-saturated porous specimens during saturation.[37] Table 1 lists the different bulk and surface wave velocities calculated for dry (air-saturated) and wet (alcohol-saturated) porous glass by neglecting viscosity. Methyl alcohol was used to saturate the porous material since the sintered glass sample happens to be somewhat hydrophobic. Also, the sound velocity in alcohol is 20% lower than in water, therefore the effect to be demonstrated is much stronger in the case of alcohol saturation. The tortuosity was taken to be 1.79, which gives the best agreement between experimental measurements and theoretical predictions for the bulk slow wave velocity in this type of porous glass[43] and was also verified by our slow wave velocity measurements in the air-filled material. On the dry sample, the surface wave velocity is approximately 8% lower than the shear wave velocity, regardless whether the surface pores are open or closed. On the wet sample, the surface wave velocity is very sensitive to the boundary conditions. For open pores, the surface wave velocity is again approximately 8% lower than the shear velocity, although both velocities are somewhat lower than in the dry sample due to the added inertia of the saturating fluid. On the other hand, for closed pores, the velocity of the true surface wave becomes as much as 40% lower than the shear velocity when the sample is wet.

Table 1 Calculated sound velocities in dry and wet porous glass.

wave mode	dry	wet
fast wave [m/s]	2,383	2,529
slow wave [m/s]	254	766
shear wave [m/s]	1,346	1,308
surface wave		
- open pores [m/s]	1,242[a]	1,209[b]
- closed pores [m/s]	1,241[a]	745[c]

[a]Rayleigh mode
[b]pseudo-Rayleigh mode
[c]slow surface mode

Figure 12 showed the schematic diagram of the experimental arrangement used in this

study. The transmitter was driven by a tone-burst of three cycles at 100 kHz. The normal component of the surface vibration was measured by a laser interferometer at two locations separated by 10 mm along the propagation direction. At both axial positions, the laser beam was scanned by ±5 mm in the lateral direction so that spatial averaging can be used to improve the accuracy of the measurement. Figure 14 shows the time- and spatial-averaged signals for a cemented glass bead sample (Grade 55, Eaton Products) after 5 hours of saturation from the bottom by methyl alcohol. Although the propagation delay is significantly less than the total length of the signal, it can be very accurately determined by calculating the cross-correlation function of the two signals. Figure 15 shows the surface wave velocity and attenuation coefficient as functions of saturation time. Owing to the low viscosity of methyl alcohol, more or less complete saturation is reached within a few seconds after the bottom of the 1"-thick sample is soaked. As a result, the velocity quickly drops from 1,240 to 1,090 m/s and the attenuation increases by almost a factor of two. At this point, the slow wave propagation is still very weak since some of the pores are clogged by trapped air bubbles. At room temperature and atmospheric pressure, it takes approximately one hour for the alcohol to dissolve the remanent air bubbles thereby opening the blocked pore channels. During this period, the surface wave velocity drops to 840 m/s and the attenuation coefficient increases to 1.1 dB/mm.

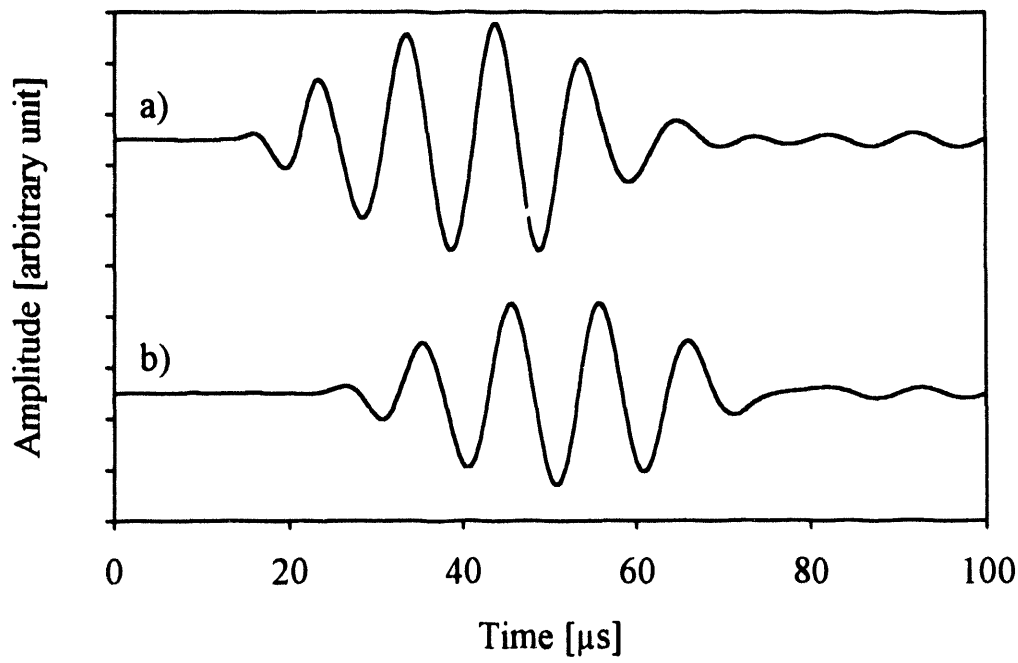

Figure 14 Detected signals at (a) 10 mm and (b) 20 mm (+10 dB gain) from the transmitter.

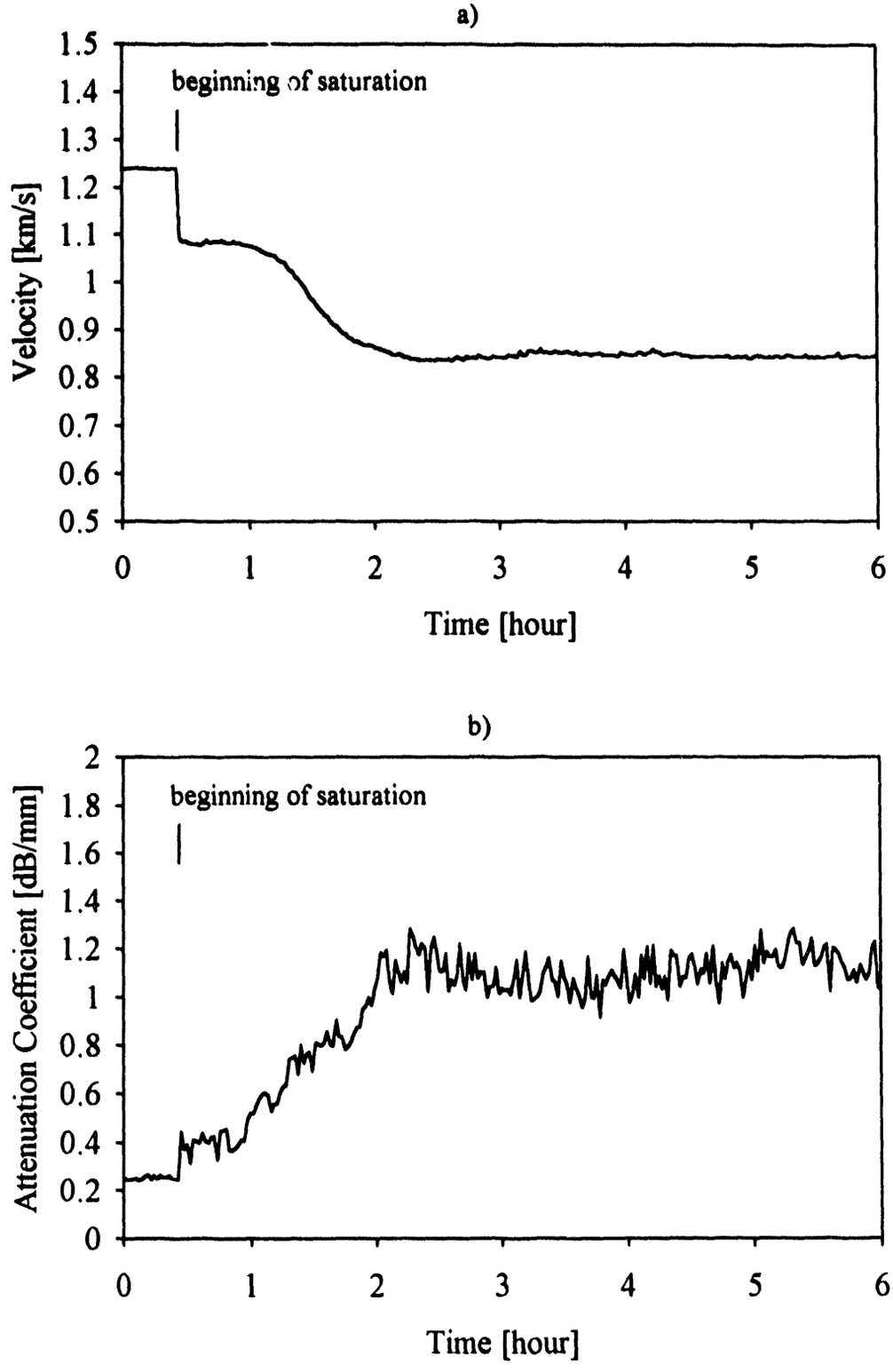

Figure 15 Surface wave velocity (a) and attenuation coefficient (b) versus saturation time for a grade 55 porous glass specimen soaked with methyl alcohol at 100 kHz.

The measured slow surface wave velocity is approximately 13% higher than expected (see Table 1). A slight discrepancy is expected due to our overestimation of the stiffness of the surface membrane by neglecting the effect of the wetting fluid covering the surface of the sample, but an even more significant experimental error might be caused by the imperfect resolution of the received signal. Theory predicts that there are two surface modes propagating on the free surface of a fluid-saturated porous solid with closed surface pores: the pseudo-Rayleigh mode, which leaks into the slow compressional mode, and the true slow surface mode. Naturally, in the case of a (not ideally free but) air-loaded surface, there is a third interface mode, namely the Stoneley mode, with a very low velocity of less than the compressional wave velocity in air. Furthermore, both pseudo-Rayleigh and "true" slow surface modes become slightly leaky into the air, but this effect is negligible for all practical purposes because of the large density difference between the fluid-saturated solid and air. Due to the same density difference, the neglected Stoneley wave is but very weakly coupled to the solid and represents a compressional wave propagating essentially in the air only along the surface. Obviously, the slow surface wave is very strongly attenuated by viscous losses therefore the added contribution of the leaky-Rayleigh mode cannot be simply neglected in the total surface vibration, although its is also strongly attenuated by viscous drag. In an ideal experiment, either the propagation length or the bandwidth of the ultrasonic pulse is chosen so high that the two arrivals are well separated in time at the point of observation. In practice, because of the tremendous attenuation in the fluid-saturated material, neither parameter can be increased without decreasing the other and full separation of the leaky-Rayleigh and slow surface waves cannot be achieved.

For example, in the above described experiment, we had to reduce the ultrasonic frequency to 100 kHz to assure a meager 10-20 mm propagation length without unacceptably high attenuation. At these values, the difference in the time of arrival is only on the order of 10 μs, i. e., much less than the total length of the tone-burst (see Figure 14). In this way, we had to evaluate a composite signal dominated by the slow surface mode but also containing a significant leaky-Rayleigh component. It can be shown that the apparent phase velocity of such a composite signal is approximately the weighted average of the velocities of the two components.[44] Since the velocity of the Rayleigh wave drops by only a few percents during saturation, the observed large overall drop in the composite surface wave velocity clearly demonstrates the dominance of the slow surface mode. Still, the presence of the unresolved leaky-Rayleigh wave can cause a substantial overestimation in the measured surface wave velocity and is probably responsible for the observed slight discrepancy. The same mechanism is also responsible for the apparent anomaly observed in the attenuation, which increases throughout the saturation process. One would expect that the slow surface and bulk waves monotonically increase as saturation progresses. Still, the

observed surface wave amplitude continues to decrease because of the decline of the initially dominating Rayleigh wave component until full saturation is reached and the slow surface wave takes over.

The above explanation is corroborated by our analytical investigation. Based on the approach described in Feng and Johnson's second paper,[33] we calculated Green's function for the free surface of a fluid-saturated porous solid with closed surface pores. Figure 16 shows the theoretical prediction for dry and alcohol-saturated porous glass bead specimens at 10 mm propagation distance. In the case of the dry specimen, there is but one surface mode, namely the ordinary Rayleigh wave. When the sample is saturated with alcohol, the Rayleigh wave becomes leaky into the slow compressional mode. Theoretically, there is a small decrease in velocity due to fluid saturation, but the slight change in the time of arrival is negligible in the presence of a much stronger effect observed in the amplitude of the signal. Due to the leaky effect, there is a strong attenuation that increases with frequency. As a result, the high-frequency components of the Rayleigh wave are essentially eliminated over the 10 mm propagation length. At the same time, there appears a slow surface wave approximately 5 μs after the Rayleigh pulse (the small bump at app. 4 μs is due to the fast wave arrival).

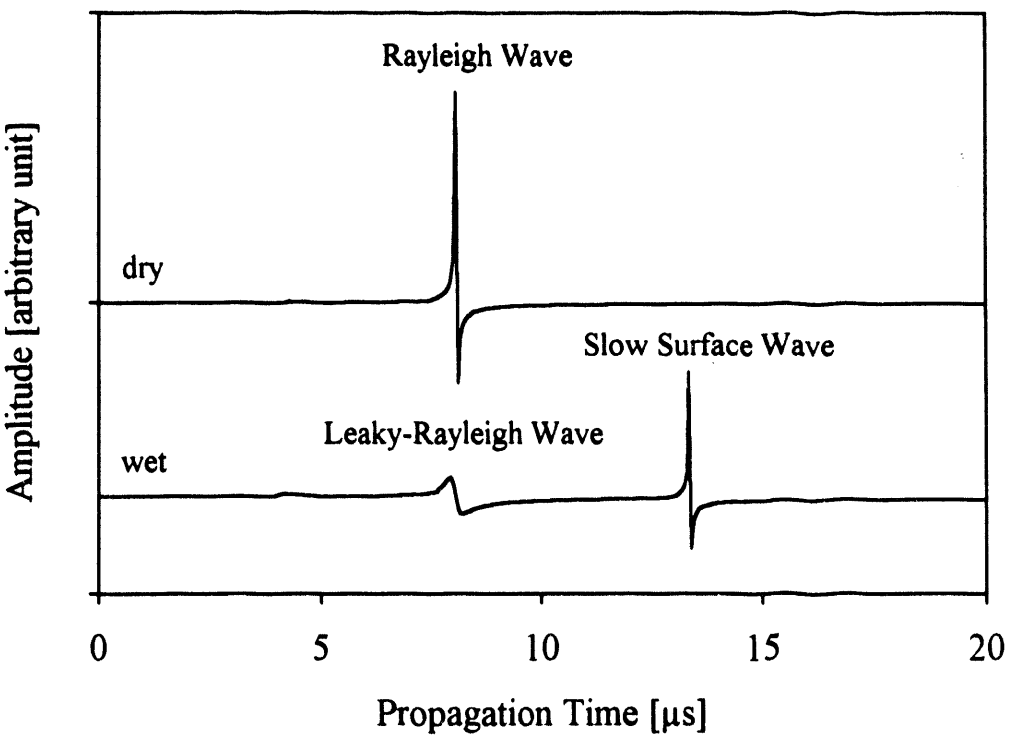

Figure 16 Theoretical prediction for Green's function on the free surface of dry and alcohol-saturated porous glass bead specimens at 10 mm propagation distance.

Figure 17 shows the theoretical prediction for the surface vibration on the free surface of dry and alcohol-saturated porous glass bead specimens at 10 mm propagation distance in the case of a five-cycle-long tone-burst of 100 kHz. These signals were simply calculated by convolving the Green's functions showed in Figure 16 by a band-pass filtered tone-burst of similar parameters used in the actual experiment. Since the separation between the leaky-Rayleigh and slow surface wave arrivals is much shorter than the total length of the pulse, only one composite signal can be observed. The apparent velocity of this signal is the weighted average of the leaky-Rayleigh and slow surface wave velocities. Our experiments showed that the actual velocity is fairly close to the value expected for the slow surface wave indicating that the contribution of the leaky Rayleigh wave is secondary in the total surface vibration. Because of analytical complications,[33] attenuation mechanisms cannot be directly incorporated into these Green's function calculations and additional theoretical efforts are needed to bring the experimental observations and the analytical predictions into better agreement. Such efforts will be outlined in more detail in the subsequent proposal.

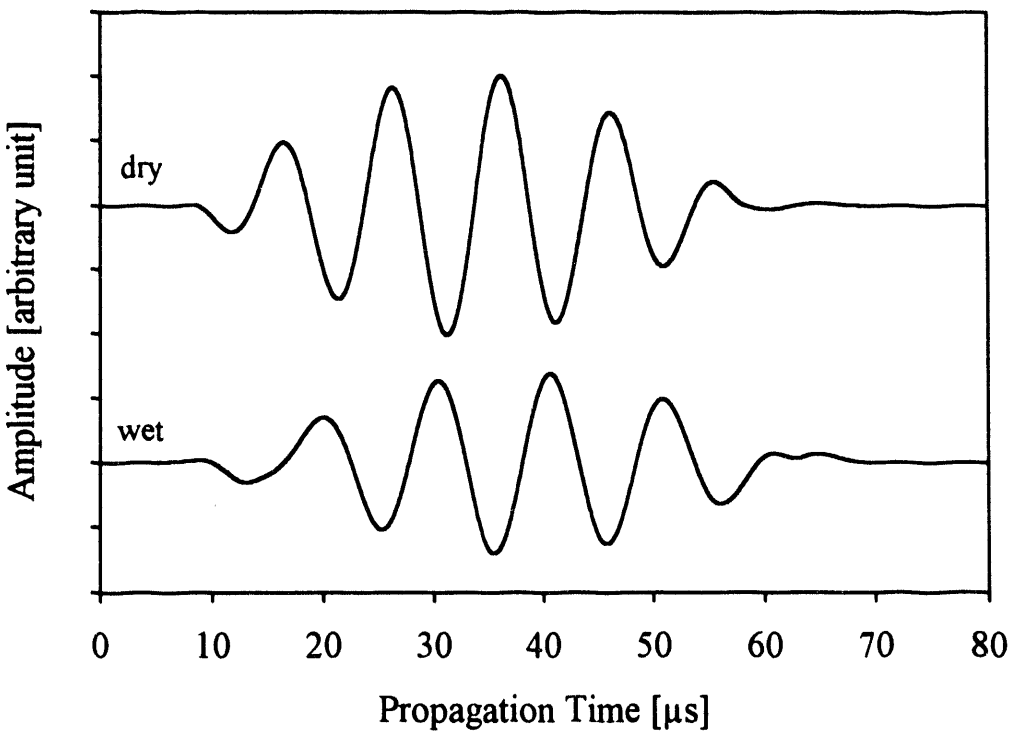

Figure 17 Theoretical prediction for the surface vibration on the free surface of dry and alcohol-saturated porous glass bead specimens at 10 mm propagation distance in the case of a five-cycle-long tone-burst of 100 kHz.

1.2.3 SURFACE STIFFNESS MEASUREMENTS

Our surface wave measurements provide circumstantial evidence that the surface pores are essentially closed by surface tension between the wetting and non-wetting fluids at the air-loaded surface of a liquid-saturated porous solid of moderate permeability. The main purpose of this part of our study was to independently verify that capillary forces can extend an ideally thin membrane over the surface pores of a fluid-saturated permeable solid at the boundary with a non-wetting fluid, which is stiff enough to assure closed-pore boundary conditions at the surface. Unfortunately, there are no sufficiently accurate and experimentally verified analytical results available in the literature for the surface stiffness of fluid-saturated porous solids of different formations. In a recent paper, we considered the simple case of cylindrical pores.[37] The geometrical configuration of a single surface pore and the curved boundary between the non-wetting superstrate fluid and the saturating substrate fluid are shown in Figure 18.

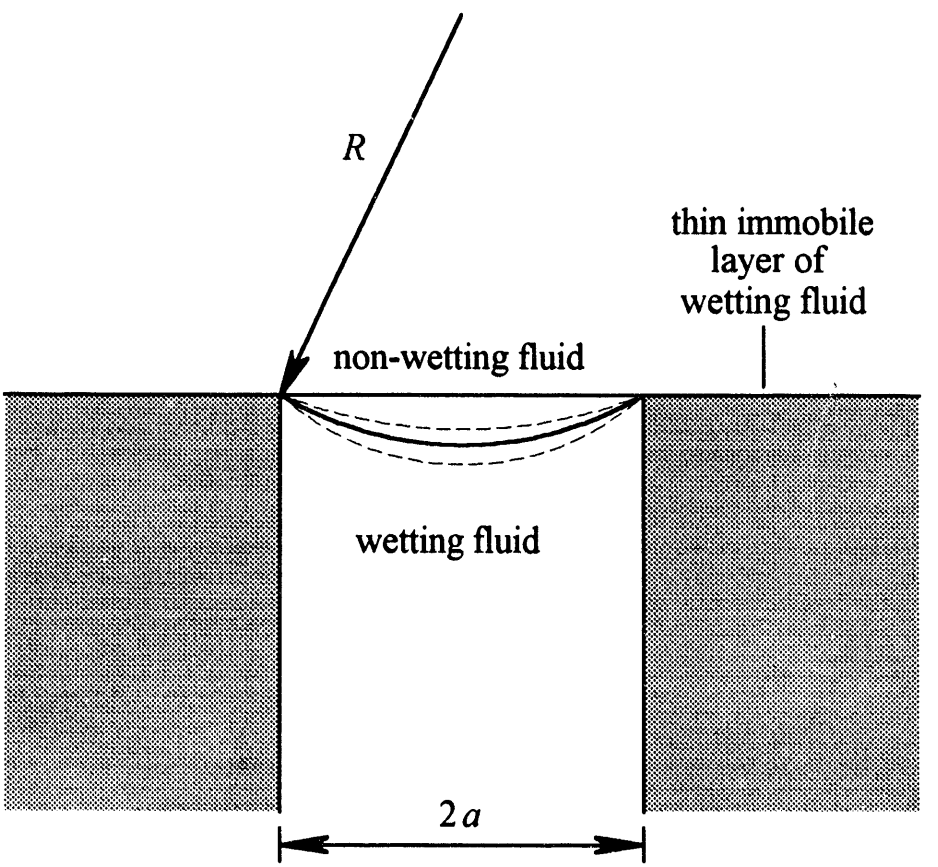

Figure 18 Schematic diagram of the boundary between a non-wetting fluid and a fluid-saturated porous solid with cylindrical pores.

According to the Laplace equation, the radius of the surface membrane is

$$R = 2\sigma / p_b, \tag{14}$$

where σ denotes the surface tension and p_b is the pressure difference at the boundary. In our case, $p_b = p_o - dp$, where p_0 is the hydrostatic pressure of the fluid filling the capillary pores and dp is a small dynamic component representing the acoustic pressure. Although there is usually a thin layer of liquid wetting the entire surface of the sample, for the sake of simplicity, we assume that the thickness of this layer is so small that viscosity keeps the fluid in it immobile and the meniscus is co-planar with the surface of the sample. The acoustic pressure changes the fluid volume in the pore by $dV = dp\ \partial R/\partial p\ \partial V/\partial R$, where $\partial R/\partial p$ can be easily determined from Equation 14 as $R^2/2\sigma$. From simple geometrical considerations,

$$\partial V/\partial R = \pi a^4/4R^2\ [1 + 0(a^2/R^2)], \tag{15}$$

where a denotes the pore radius. Assuming that the static pressure acting on the interface is much lower than the maximum capillary pressure, $R >> a$ and Equation 15 can be approximated by its first term only. Consequently,

$$dV = dp a^4 \pi / 8\sigma. \tag{16}$$

Here, the pressure difference between the wetting and non-wetting fluids is $dp = p - p'$ and the relative displacement of the wetting fluid with respect to the solid frame is $U_n - u_n = dV/\pi a^2$. By substituting Equation 16 into the definition of the surface stiffness previously given by Equation 13, we get $T_s = 8\sigma/\phi a^2$. For a network of cylindrical pores, the combination of the Darcy and Poiseuille laws gives $\kappa_o = \phi a^2/8$ for the static permeability. This well-known formula can be used to approximate the surface stiffness as[37]

$$T_s = \sigma/\kappa_o. \tag{17}$$

For water in contact with air, $\sigma \approx 7.3\ 10^{-2}$ N/m,[45] and even a relatively high static permeability of $\kappa_0 = 10$ Darcy $\approx 10^{-11}$ m^2 produces a surface stiffness in excess of 10^9 N/m^3. A quick comparison with Figure 11 verifies that, for all practical purposes, the pores are sealed under such conditions.

Equation 17 establishes a very simple inverse relationship between the surface stiffness and the static permeability of the permeable solid in the case of cylindrical pores. One major drawback of this model is that it gives permeability only in one direction. To overcome this difficulty, the model is usually modified so that only one-third of the capillary tubes are placed in each of three mutually orthogonal directions. This leads to a three-times reduction in both permeability and surface stiffness for the same pore radius and porosity without affecting their ratio expressed in Equation 17. Similar relationships for other regular formations, such as ordered or randomly packed spherical beads are much more difficult to obtain. As the pore shape becomes more irregular the permeability is determined by the smallest cross-sections causing viscous friction while the surface stiffness depends more on the largest dimensions dominating the compliance of the surface membranes. Still, for a given pore shape, both the surface compliance $1/T_s$ and the static permeability κ_0 are proportional to the square of the characteristic pore size, and Equation 17 is expected to take the more general form of

$$T_s = s\sigma/\kappa_o, \tag{18}$$

where s denotes a shape factor which becomes much less than one as the pore structure becomes more irregular and random.

The schematic diagram of our recently developed experimental arrangement is shown in Figure 19. The technique is based on the direct measurement of the average surface displacement of the water-saturated specimen upon changing the hydrostatic pressure in the capillary pores. The porous specimen is soaked from below by water. The fluid level in the pores can rise to a maximum capillary height of $h_c = p_c/\rho_w g$, where p_c denotes the maximum capillary pressure accommodated by the given pore structure and the surface tension of the wetting fluid, ρ_w is the density of the fluid and g denotes the gravitational acceleration. The pressure difference between the air and the water at the surface is changed by increasing and decreasing the water level in the tank. This is achieved simply by moving an external water tank mounted on a computer controlled translation stage. This external reservoir is connected to the measuring tank by a flexible rubber tube. The water level in the tank is always kept at least a few millimeters below the surface of the saturated specimen and never lowered more than one-third of the experimentally determined maximum capillary height h_c for a given specimen so that full saturation of the specimen can be maintained throughout the experiment. In this way, the microscopic interface membranes formed over the surface pores are kept intact but strained sufficiently to produce a measurable surface displacement on the order of a few microns.

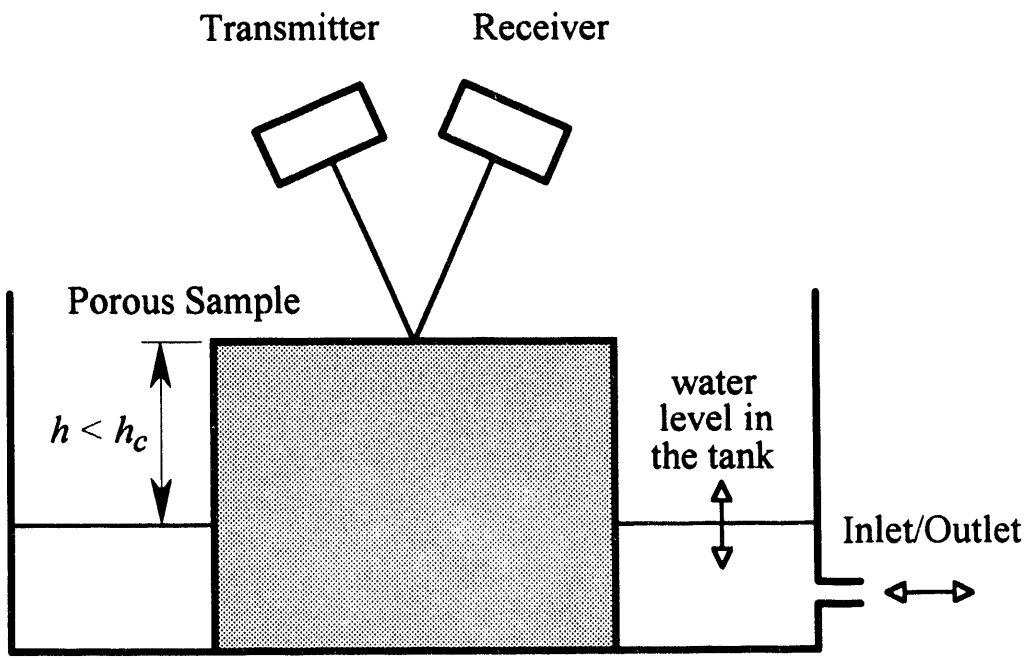

Figure 19 Schematic diagram of the experimental arrangement for static surface stiffness measurements.

The average surface displacement is directly measured by an ultrasonic transmitter-receiver pair working at $f = 100$ kHz. Because of the very high acoustic impedance of water with respect to air, the top surface of the porous skeleton and the capillary membranes present a continuous, essentially rigid reflecting interface to the incident air-borne ultrasonic pulse. Since the acoustic wavelength $\lambda \approx 3.3$ mm is significantly larger than the combined surface roughness H of this interface, the received signal from the surface appears to be reflected from a plane reflector positioned at the average height of the slightly irregular surface. The inherent surface roughness of the reflecting interface manifests itself through a small scattering induced loss[23]

$$L\,[\mathrm{dB}] \approx 17.4\,[2\cos(\theta_i)\,\pi H/\lambda]^2, \tag{19}$$

where θ_i denotes the angle of incidence of the acoustic beam. The measured phase modulation of the reflected signal $\Delta\varphi$ can be expressed by the average surface displacement ΔU as follows

$$\Delta\varphi = 4\pi\cos(\theta_i)\,\Delta U/\lambda\,. \tag{20}$$

The porous solid is rigidly mounted so that the changing buoyancy of the specimen cannot produce any displacement of the skeleton (u_n=0) and the average surface displacement ΔU is entirely due to the water level rising and falling in the surface pores $\Delta U = \phi U_n$. The pressure difference between the air and the water at the interface is periodically changed by $\Delta p = \Delta h \rho_w g$. Finally, the surface stiffness can be directly calculated from the measured average surface displacement as $T_s = \Delta p / \Delta U$.

Theoretically, the pressure modulation Δp is limited only by the maximum capillary height, h_c. In practice, the actual change in the water level Δh was always kept below 20 mm, i. e., Δp was less then 200 N/m^2. Under these conditions, the maximum measurable surface stiffness is limited by the accuracy of the phase measurement. Naturally, this accuracy is greatly dependent on the ultrasonic frequency used to monitor the surface motion. We found, that the optimum frequency was around 100 kHz. At lower frequencies, the inevitable uncertainties of the phase measurement translated into increasingly high displacement errors. At higher frequencies, the surface roughness induced attenuation of the reflected signal starts to produce significant amplitude modulation which interferes with the phase measurement.

The block diagram of the computer controlled measuring system was shown in Figure 6. We used a pair of Panametrics V101 1-inch-diameter contact transducers to generate and receive the ultrasonic signals. These transducers have a resonance frequency of 500 kHz below which they offer a fairly flat frequency response down to 50 kHz and have been successfully used in previous experiments to generate and detect air-borne ultrasonic waves. After the optimum inspection frequency was established around 100 kHz, both transducers were equipped with a 6-mm-thick (quarter-wavelength) Plexiglas matching plate to increase their sensitivity in the narrow frequency band actually used during the measurements. The transmitter was driven by a twenty-cycle-long tone-burst of 100 kHz carrier frequency. This signal was generated by a very stable quartz synchronized WAAG waveform synthesizer computer board plugged into the 486 PC controlling the measuring system. In order to achieve maximum signal-to-noise ratio, the driver signal was further amplified by an ENI 240L power amplifier to approximately 100 V_{pp}. The received signal was first boosted by a Panametrics 5678 preamplifier and than fed into an 8-bit digital-to-analog converter through a filter. There the signal was first averaged a 1000 times to eliminate electrical noise and then Fourier transformed. Finally, the measured amplitude and phase at the carrier frequency was stored for further analysis.

As an example, Figure 20 shows a typical ultrasonic signal received from a cemented glass bead specimen at 35° angle of incidence. The first signal is the direct reflection of the transmitted pulse from the surface of the water-saturated specimen. Since both receiver and transmitter act like reflectors, there will be a train of pulses following the first arrival. For example, the second arrival at the receiver is the pulse which has been reflected from the surface of the specimen three times. Naturally, high sensitivity to microscopic fluid displacements requires very accurate phase measurements on the received signal. In order to increase the signal-to-noise ratio we chose a tone-burst as long as allowed by the arrival of the third reflection and applied a band-pass filter to reject electrical noise beyond the narrow detection bandwidth. As a result, the signal exhibits relatively slow exponentially decaying transients at the beginning and the end, but the phase measurements were carried out on the steady-state central part of the signal. The total propagation distance from the transmitter to the specimen and back to the receiver (≈70 mm) was chosen to be as small as possible within the limitations of the given geometrical configuration. This is necessary to reduce the adverse effect of changing sound velocity in the air on the

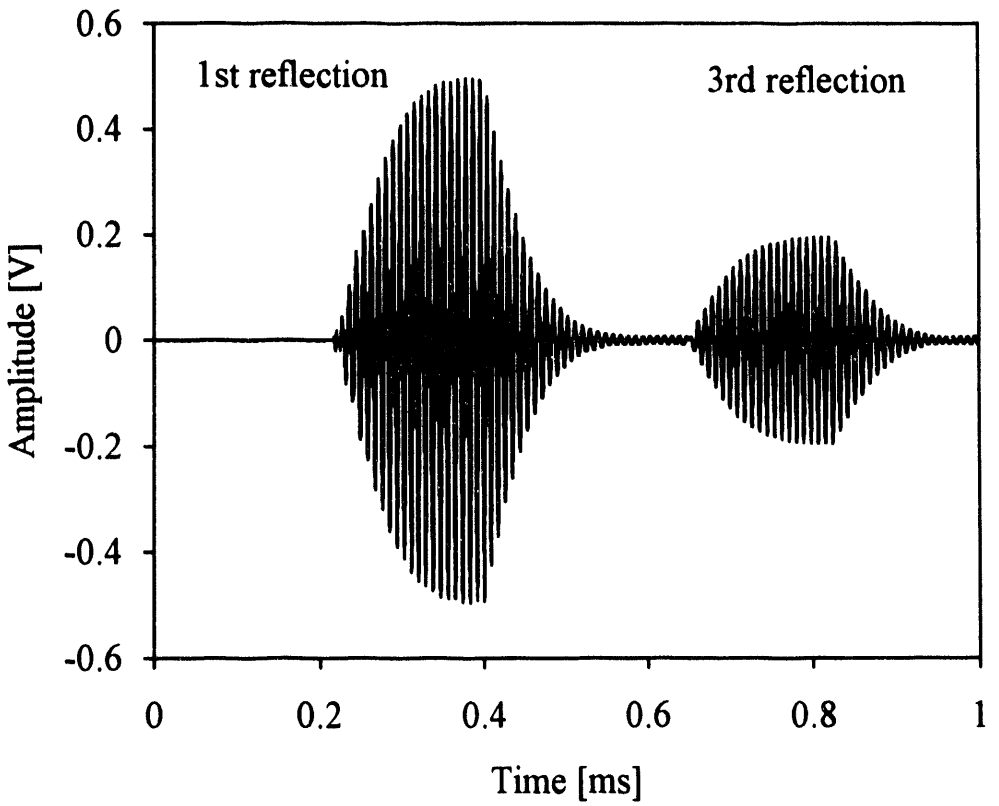

Figure 20 Typical ultrasonic signal received from a cemented glass bead specimen at 35° angle of incidence.

accuracy of the phase measurement. We placed the measuring tank into a simple environmental chamber which kept the temperature and the relative humidity at constant levels of 70 ^{o}F and 100%, respectively, and eliminated air turbulence. In spite of these efforts, the phase of the received signal showed roughly 1^{o} long-term drift over the approximately 10-hour period of the whole measurement. This inherent instability translates into approximately $\Delta U \approx 5$ μm surface displacement at 100 kHz. Since the change in the interface pressure is limited to $\Delta p \approx 200$ N/m^2, the largest surface stiffness measurable in a long-term static experiment is around $4\ 10^7$ N/m^3.

Fortunately, single phase measurements can be made as fast as every 20 second and the settling time of the water level is not more than 1 minute. This relatively fast response was exploited to further increase the measuring sensitivity and accuracy by averaging. The water level in the measuring water tank was controlled by alternatingly lifting and lowering a connected external tank in four steps according to the staircase function shown in Figure 21.a (the actual change of the water level in the measuring tank was calculated by the computer from the displacement of the external tank and the calibrated ratio between them). Figure 21.b shows the measured phase modulation of the reflected signal for a Grade 175 cemented glass bead specimen (Eaton Products) over a period of 5 hours (a full measuring cycle includes 80 consecutive data points and takes approximately half an hour). Although there is a significant experimental uncertainty superimposed on the measured phase modulation, the effect of the moving surface membranes is quite obvious in this raw data, too. Figure 21.c shows the measured amplitude modulation from the same specimen. As one can expect from Equation 19, the amplitude modulation seems to be proportional to the square of the membrane displacement. In comparison, the phase modulation appears to be a more or less linear function of the pressure, which indicates that the surface stiffness caused by capillary forces is an essentially linear parameter. In this case, the amplitude modulation was approximately 0.2 dB peak-to-peak which had a negligible effect on the phase measurement. In all other cases, the grain size of the porous solid was smaller and the side effect caused by the amplitude modulation was even less.

In order to further reduce the uncertainty of the experimental results, the raw data was collected over a period of 10-20 hours and subsequently averaged by the computer. Figure 22a shows the averaged experimental phase modulation over 40 cycles and the best fitting staircase function for the same Grade 175 glass bead specimen. From the least squares fitting, the phase modulation was determined as 3.58^{o} corresponding to $\Delta U \approx 20$ μm average surface displacement. Naturally, less permeable samples produced much smaller surface displacements even when we increased the pressure modulation. As an other example, Figure 22b shows the averaged experimental phase modulation over 40 cycles and the best fitting staircase function for

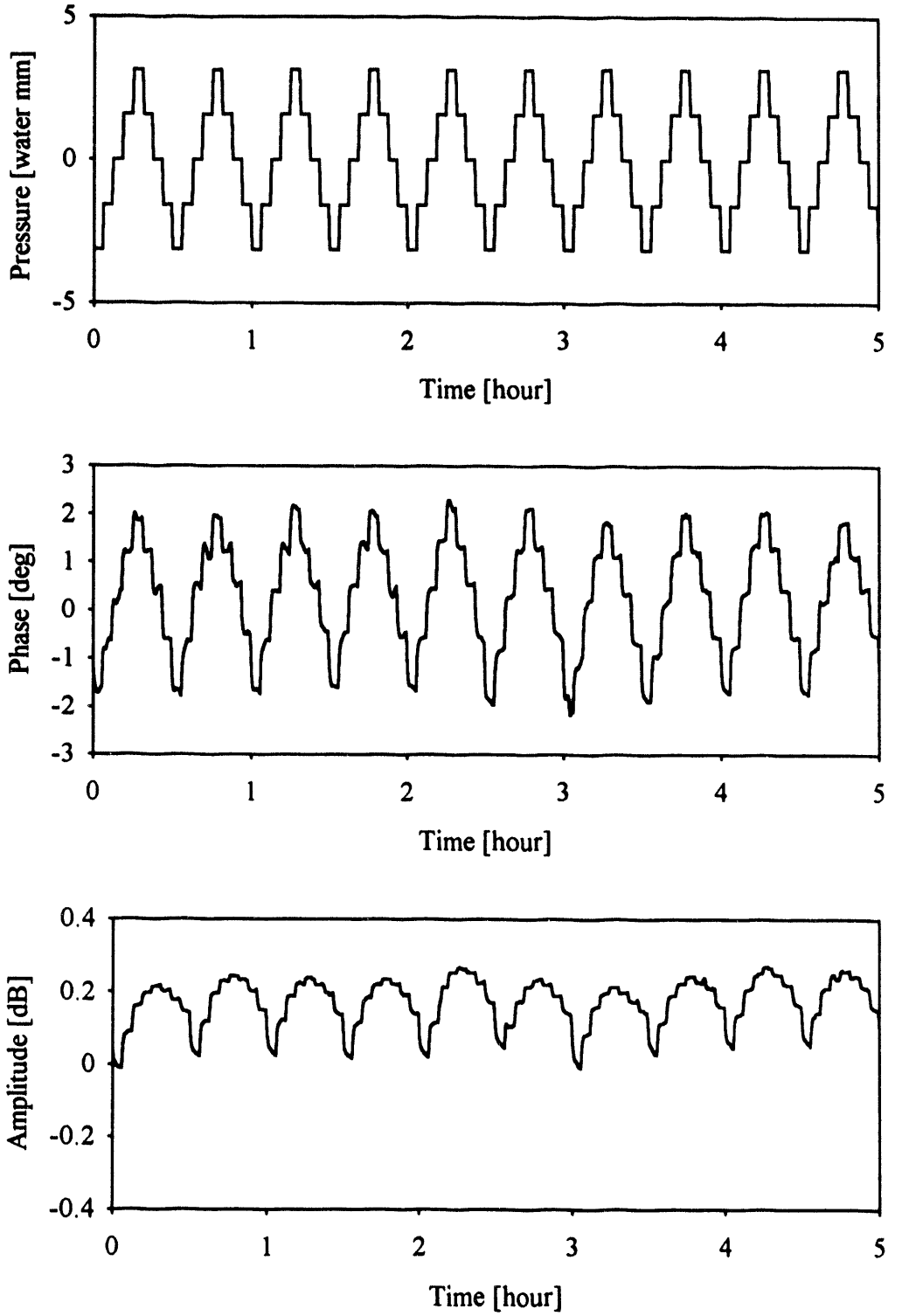

Figure 21 Examples of the (a) hydrostatic pressure, (b) phase, and (c) amplitude modulation (Grade 175 cemented glass bead specimen).

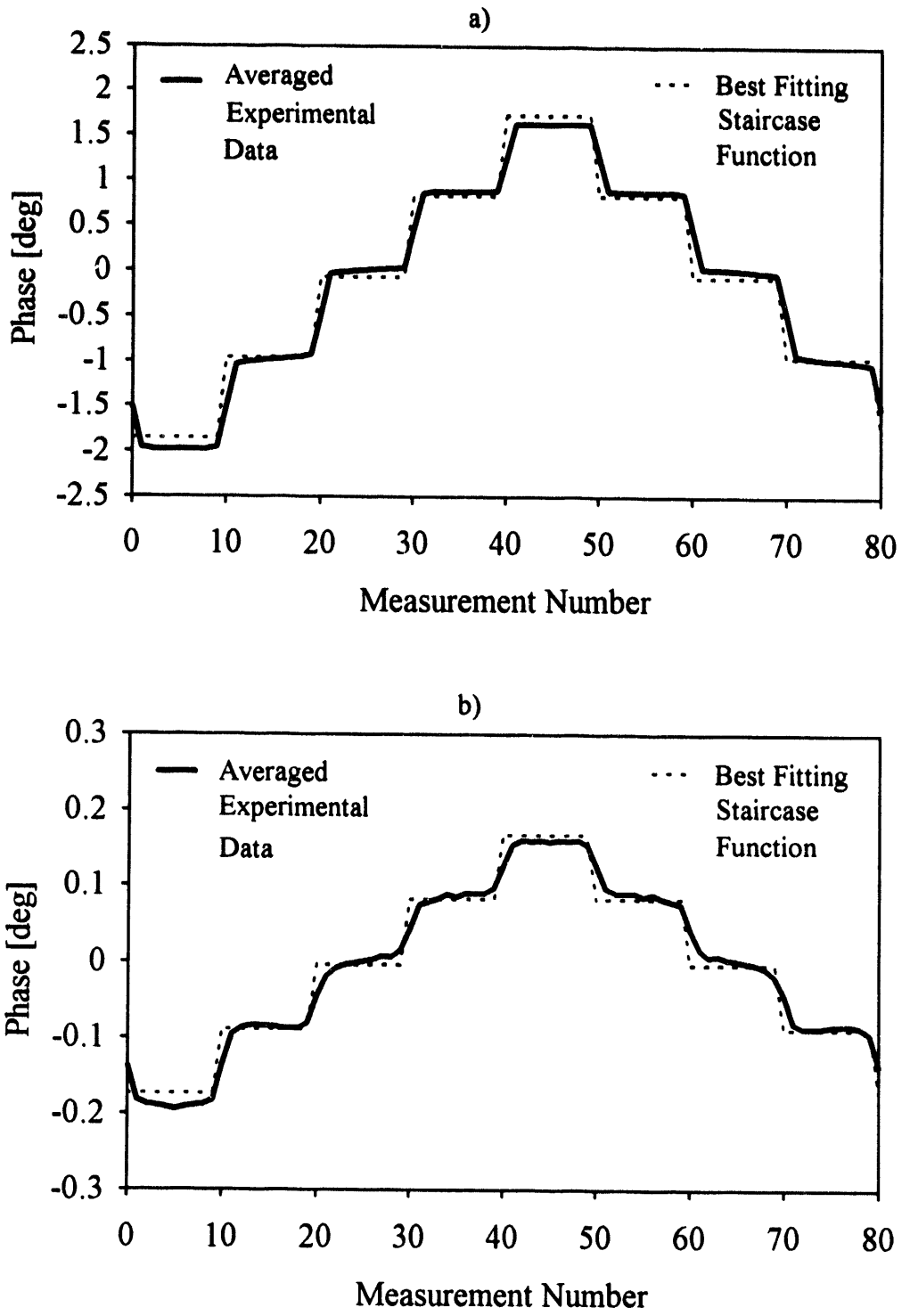

Figure 22 Examples of the averaged experimental phase modulation and the best fitting staircase functions for cemented glass bead specimens of (a) Grade 175 at Δh = 6.3 mm and (b) Grade 15 at Δh = 19.5 mm (full cycle takes app. 30 minutes).

a Grade 15 glass bead specimen at Δh = 19.5 mm modulation level. The phase modulation is only 0.34° corresponding to $\Delta U \approx 1.9$ μm average surface displacement. In order to establish the detection threshold of our acoustic displacement sensor, we also measured the apparent surface stiffness of a non-permeable Plexiglas plate. We found that, thanks to the extensive averaging used in the evaluation of the raw data, the noise floor of the phase measurement was below 0.01°, which corresponds to a displacement threshold of less than 60 nm. Combined with the previously given $\Delta p \approx 200$ N/m^2 maximum pressure modulation, this sensitivity assures accurate surface stiffness measurement up to approximately 3 10^8 N/m^3.

According to our theoretical predictions, the surface stiffness is independent of the static pressure, i. e., independent of the level of water in the tank. We have mentioned in connection with Equation 15 that this is true only when $R >> a$, i. e., the static pressure acting on the interface is much lower than the maximum capillary pressure. The validity of this assumption as well as the accuracy of the linear surface stiffness approximation can be established from Figure 22. The static pressure is changed in four equal steps but the corresponding phase steps are not quite equal indicating that the fluid displacement is not strictly proportional to the pressure. The surface stiffness appears to be roughly 30 % higher in the first (lowest pressure) step of the four-step cycle than in the last (highest pressure) step. This strong nonlinearity has to be taken into consideration in the evaluation of the experimental data since it might cause significant underestimation in the measured surface stiffness.

The main goal of this part of our experimental effort was to demonstrate that the surface stiffness produced by capillary forces is sufficiently high to produce "closed-pore" boundary conditions at the interface between air and typical water-saturated porous specimens. In addition, we hoped to confirm the quantitative predictions of the analytical model for cylindrical pores and to verify the simple qualitative relationship of Equation 18 between surface stiffness and static permeability for self-similar porous structures such as spherical glass beads of different grain sizes. Table 2 lists the different porous samples used in this study and their main parameters.

Since analytical results are currently unavailable for the surface stiffness of porous formations with other than aligned cylindrical pores, we have prepared a simple model specimen to verify our theoretical prediction that the surface stiffness is equal to the ratio of the surface tension between the saturating and non-wetting superstrate fluids and the permeability of the specimen. This model was made of Plexiglas and contained 200 1-mm-diameter drilled holes more or less randomly distributed over an area of approximately 2 square-inches. The porosity of this

Table 2 List of the materials used in this study and their main properties.

Material	Porosity ϕ [%]	Permeability κ_0 [10^{-12} m^2]	Pore Radius a [10^{-6} m]
Plexiglas plate with drilled cylindrical holes	19	5900[a]	500
Porous glass, Grade 175[b]	30	67	87.5
Porous glass, Grade 90[b]	30	27	45
Porous glass, Grade 55[b]	30	11	27.5
Porous glass, Grade 40[b]	30	6.5	20
Porous glass, Grade 15[b]	30	2.2	7.5
Berea Sandstone	14	0.45[c]	n/a

[a] calculated from $\kappa_o = \phi a^2 / 8$

[b] cemented spherical glass beads made by Eaton Products, all parameters are from the manufacturer's specification, pore radius refers to the maximum interstitial pore diameter

[c] measured at the Lawrence Livermore National Laboratory

model was estimated at $\phi \approx 19\%$. The static permeability was calculated from $\kappa_o = \phi a^2 / 8$ as $5.9\ 10^{-9}$ m^2. We measured the surface stiffness of this specimen by the previously described acoustic technique and found it to be $T_s \approx 6.3\ 10^6$ N/m^3. Based on the previously mentioned tabulated value of $\sigma \approx 7.3\ 10^{-2}$ N/m for the surface tension between water and air, the theoretically predicted surface stiffness (Eq. 17) is $1.24\ 10^7$ N/m^3, i. e., roughly two times higher than the experimentally determined value. Considering the crude approximations made in deriving

the theoretical result and the experimental uncertainties in the measured surface stiffness, the agreement is quite good. In particular, the assumption that the fluid moves only in the pores while it is kept completely immobile by its viscosity in the continuous thin layer covering the top of the frame is open for suspicion. Fluid motion in this layer can give a significant contribution to the total surface compliance and might be responsible for the measured lower surface stiffness. Another important factor which might contribute to lowering the measured surface stiffness is the previously discussed nonlinearity of the surface membrane. This membrane appears to be the "softening" type, i. e., its stiffness decreases with increasing pressure. We have mentioned above that the initial stiffness measured at the lowest pressure level of the four-step cycle is typically 30% higher than the one measured at the highest pressure level. This nonlinear effect itself can be responsible for roughly 15% reduction in the measured average surface stiffness with respect to the predicted value.

In order to test the accuracy of the general relationship between surface stiffness and static permeability (Eq. 18) and to determine the shape factor s for a more common pore geometry other than cylindrical pores, we have measured the surface stiffness of different water-saturated cemented glass bead specimens manufactured by Eaton Products International, Inc. EP Brand Porous Structures are porous engineering materials consisting of tiny, precisely-sized spherical particles rigidly bonded together. These samples have an evenly distributed network of interstitial pores which are of uniform size, completely open and interconnected. This material is available in five standard grades which also denote the maximum interstitial pore diameter in microns. Because of the self-similar nature of this material and the more than one order of magnitude size-range covered by the five standard grades, it is especially suitable to test the validity of the general relationship between surface stiffness and static permeability for a given pore geometry and to find an empirical estimate for the shape factor in the case of spherical grains.

Figure 23 shows the measured surface stiffness as a function of interstitial pore diameter in cemented glass bead specimens for five different grades. From theoretical considerations, one would expect that the surface stiffness is inversely proportional to the square of the interstitial pore diameter. Instead, the experimental data seems to indicate a significantly lower power of 1.45. Interestingly, the same anomaly can be observed in the relationship between static permeability and pore size, too. As a result, the surface stiffness is still inversely proportional to the static permeability, as it is demonstrated in Figure 24. Here, we plotted the shape factor as a function of the static permeability. The shape factor can be readily calculated from Equation 18. Over the wide permeability range of approximately one and a half decade represented by these five standard grades, the shape factor is constant at $s \approx 2.7\ 10^{-3}$ within ±15%. In comparison, for

a porous structure of cylindrical pores the shape factor was found to be $s \approx 0.51$, somewhat lower than the predicted value of unit but almost two orders of magnitude higher than for spherical beads.

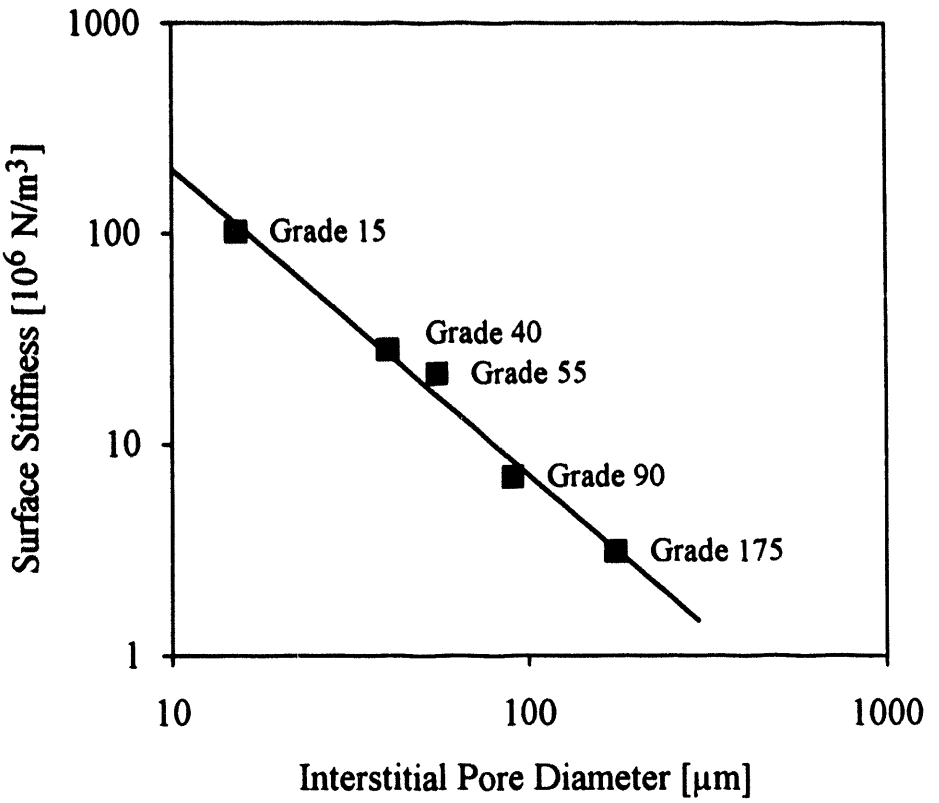

Figure 23 Measured surface stiffness versus interstitial pore diameter in cemented glass bead specimens.

This rather low shape factor can be attributed to three major effect. First, as we mentioned before, the surface stiffness is mainly determined by the largest pore diameter while the permeability is more dependent on the diameter of the smallest cross-sections, i. e., the narrow throats of the pore channels. Second, although these materials are relatively easy to machine by conventional means such as sawing, milling or lathe turning, the high rigidity of the individual glass beads combined with the relative weakness of the bond between the cemented particles often results in larger than normal surface pores caused by chipped-off beads. This effect, which is readily visible on the machined surfaces of all specimens, might significantly reduce the overall

surface stiffness of the samples. Third, the thin water layer covering all the surface beads might also further reduce the total surface stiffness. In the case of cylindrical pores, this layer is effectively cut off from the bulk of the water in the capillary pores and, especially at higher frequencies, it is kept immobile by viscosity. Obviously, further analytical efforts are needed to understand the effects causing the relatively low surface stiffness of water-saturated glass bead specimens. In spite of the more than two orders of magnitude reduction in surface stiffness compared to the case of cylindrical pores of similar static permeability, for the lower three grades, the measured stiffness is still higher than the previously determined threshold stiffness of $T_s = 10^7$ N/m^3 required to produce "closed-pore" boundary conditions on a water-saturated glass bead specimen. It is also expected that the excess compliance caused by the thin water layer covering the surface grains is a visco-elastic contribution which significantly reduces the static surface stiffness but has a negligible effect on the dynamic stiffness at ultrasonic frequencies.

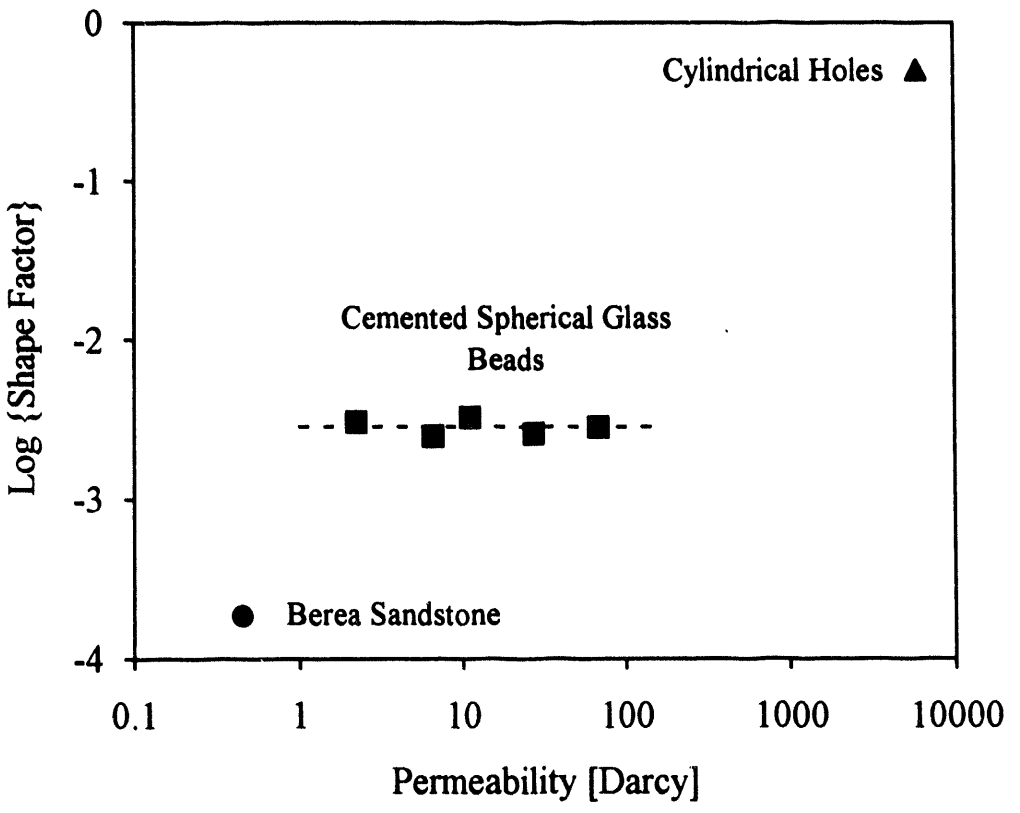

Figure 24 The product of the measured surface stiffness and the static permeability versus permeability for different porous materials.

We have also measured the surface stiffness of a water-saturated Berea sandstone specimen of 450 mD static permeability. We found that the surface stiffness was only 3 10^7 N/m^3, much less than expected based on the permeability of the specimen. The measured value corresponds to a shape factor of $s \approx 2\ 10^{-4}$ (also shown in Figure 24), i. e., roughly one order of magnitude lower than the empirical value for spherical beads. We believe that this significant reduction can be attributed to essentially the same three effects mentioned above in connection with the cemented glass bead specimens.

1.2.4 CONCLUSIONS

Our calculations showed that capillary forces can easily produce closed-pore boundary conditions at the interface between a non-wetting fluid (air) and a porous solid saturated by a wetting fluid (water). The stiffness of the membrane extended over the surface pores depends on the surface tension of the wetting fluid and the pore size and shape. We derived a simple approximation relating the boundary stiffness to the formation permeability. We found that the boundary stiffness is around 10^{10} N/m^3 in most natural rocks, i.e., well above the threshold value required to achieve closed-pore boundary conditions. Under these conditions, the Rayleigh-type surface wave becomes strongly attenuated by energy leakage into the slow compressional wave and the velocity of the true surface mode drops below the slow wave velocity. Of course, the mobility of the water is badly limited by viscous drag between the fluid and the solid frame. This effect is particularly strong in natural rocks where the drag is greatly increased by the highly irregular flow through the inhomogeneous pore structure and by inherent impurities such as submicron clay particles sticking to the pore walls and clogging the narrow throats of the pore channels.

We used the direct excitation technique to measure surface wave velocity and attenuation on both wet and dry rocks. The Rayleigh velocity of dry rocks is approximately 10% lower than their shear velocity. The surface wave velocity of water-saturated rocks of low permeability (below 100-200 mD) is 5-10% lower than the Rayleigh velocity of the dry specimen. This drop in velocity is primarily due to the added inertia of the saturating fluid, which is also apparent in the similar decrease in the shear wave velocity. The surface wave velocity of water-saturated rocks of high permeability is much lower, approximately 60-70% of the Rayleigh velocity of the dry specimen. This strong correlation between the observed surface wave velocity change caused by water-saturation and the formation permeability can be used for ultrasonic assessment of the dynamic permeability. Further investigation is needed to establish a reliable theoretical model for

the observed phenomenon and to develop inversion techniques for the quantitative evaluation of material properties from the velocity and attenuation of the slow surface wave propagating on the free surface of a fluid-saturated rock.

We further improved our experimental system by the introduction of laser interferometric detection. Thanks to a recently developed detection method, the so-called random speckle modulation technique, we successfully adapted laser interferometry to surface wave inspection of fluid-saturated permeable materials. The new technique allows us to continuously monitor surface wave propagation during the saturation process itself. The laser interferometric technique was first tested on alcohol-saturated porous ceramics. In the next step, the same approach will be adapted to water-saturated natural rocks. Our experimental results provide clear evidence of the propagation of the new "slow" surface mode on the free surface of fluid-saturated porous solids when the pores are closed at the surface by capillary forces.

In a separate effort, we studied the surface stiffness of different water-saturated porous solids by a novel acoustical method. The surface impedance of a fluid/fluid-saturated porous solid interface is defined as the ratio of the pressure difference between the fluids on the two sides of the interface and the volume velocity of the fluid through the surface pores. In most cases, the surface pores are inherently "open" and the surface impedance is negligible when the sample is fully submerged in fluid. On the other hand, due to surface tension, practically closed-pore boundary conditions can prevail at an interface between a non-wetting fluid (e. g., air) and a porous solid saturated with a wetting fluid (e. g., water). This effect is caused by the high stiffness of the microscopic fluid membranes extended by capillary forces over the otherwise open surface pores. We have determined the quasi-static surface stiffness of different water-saturated porous materials by changing the hydrostatic pressure and directly measuring the average surface displacement by an acoustical sensor. Generally, the surface stiffness is proportional to the surface tension of the wetting fluid and inversely proportional to the static permeability of the specimen. For cylindrical pores, the measured surface stiffness is in good agreement with theoretical predictions. For more irregular geometries, such as consolidated spherical beads, the surface stiffness is still inversely proportional to the static permeability but its value is orders of magnitudes lower than for cylindrical pores of comparable permeability. Two research areas of particular interest seem to require further attention in the future. First, more analytical efforts are needed to estimate the above defined shape factor of different regular and random porous formations by comparing their surface stiffness and static permeability. Second, additional experimental efforts are needed to measure the high-frequency dynamic surface stiffness of water-saturated porous specimens.

DATE
FILMED
7/1/94

END